JACS Au
AN OPEN ACCESS JOURNAL OF THE AMERICAN CHEMICAL SOCIETY

pubs.acs.org/jacsau
Article

SMAP3-ID for Identification of Endogenous Protein−Protein Interactions Reveals Regulation of Mitochondrial Activity by Lamins

Julia Warren, Jian Wang, Francis Dhoro, Bo Chao, Ashok Reddy, Stefanie Kaech Petrie, Larry L. David, Xiangshu Xiao,* and Bingbing X. Li*

Cite This: JACS Au 2025, 5, 302−319
Read Online

ACCESS | Metrics & More | Article Recommendations | Supporting Information

ABSTRACT: Proteins regulate biological functions through the formation of distinct protein complexes. Identification and characterization of these protein−protein interactions are critical to deciphering their mechanism of action. Different antibody-based or cross-linking-based methods have been developed to identify the protein−protein interactions. However, these methods require genetic engineering or other means to disrupt the native environments. To circumvent this limitation, we introduce here SMAP3-ID (small-molecule-assisted identification of protein−protein interactions through proximity) method to identify protein−protein interactions in native cellular environment. This method combines a selective ligand for binding to a protein of interest for photo-cross-linking, a live-cell-compatible bioorthogonal click reaction with a trifunctional chemical probe, and a final photo-cross-linking reaction to covalently capture the interacting proteins. Using the SMAP3-ID method and nuclear lamins as an example, we identified numerous lamin interactors in native cells. Significantly, we identified a number of mitochondrial enzymes as novel lamin A (LA) interactors. The interactions between mitochondrial enzymes and LA were further validated, which provides mechanistic insights underlying the metabolic alterations caused by mutations in LA. Furthermore, our previously described small-molecule ligand for LA, **LBL1**, also induced changes in mitochondrial activity and cellular bioenergetic organization. We conclude that SMAP3-ID is a potentially powerful and generalizable method to identify protein−protein interactions in the native cellular environment.

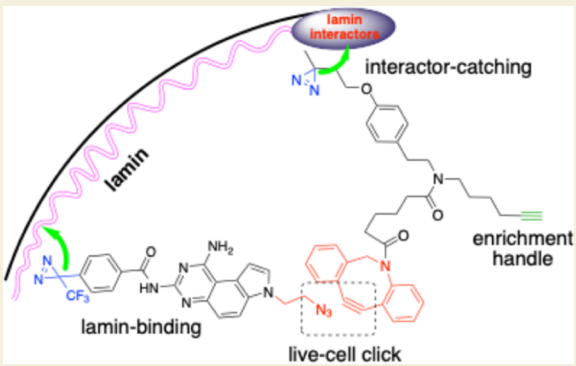

KEYWORDS: *chemoproteomics, lamin, LBL1, LBL1-PCF, mitochondria, protein−protein interaction, photo-cross-linking, SMAP3-ID*

INTRODUCTION

Protein−protein interactions (PPI) play pivotal roles in all aspects of biology. Formation of appropriate protein complexes drives fundamental physiological functions of cellular proteins.[1] They are critical for molecular processes ranging from gene transcription to protein translocation and cellular processes encompassing cell division, motility, and intercellular communications.[2] Dysregulation of the biomolecular complexes is critical to the development of different pathological diseases.[2] Therefore, there has been a great need for identifying and characterizing these subproteomes.[3] Elucidation of specific protein−protein interactions (PPIs) has propelled a paradigm shift in various disease treatment strategies, enabling the development of different therapeutic modalities including small molecules and monoclonal antibodies that target the pathological changes arising from aberrant PPIs.[4,5]

Nuclear lamins are type V intermediate filament (IF) proteins.[6] They were originally identified as detergent-and salt-insoluble proteins that resided on the inner side of nuclear membranes.[7] There are A-type and B-type lamins in mammals. The A-type lamins are encoded by *LMNA* gene with LA and LC as the two alternatively spliced products, while the B-type lamins consist of LB1 and LB2 encoded by *LMNB1* and *LMNB2*, respectively.[6] The lamins form a mesh-like protein network underneath the inner nuclear envelope to support the mechanical stability of the cell nucleus.[6,8] In addition to their function as nuclear structural components, lamins also play essential roles in many other cellular processes. These include regulation of DNA replication, DNA damage repair, chromatin regulation, DNA transcription, stem cell regulation, and mechanotransduction.[6,9−13] Due to their multifaceted roles in various biological processes, many disease pathologies are linked to mutations in lamin genes. For example, over 450 mutations of LA have been reported to cause a wide spectrum of diseases collectively known as laminopathies including

Received: October 18, 2024
Revised: January 2, 2025
Accepted: January 3, 2025
Published: January 14, 2025

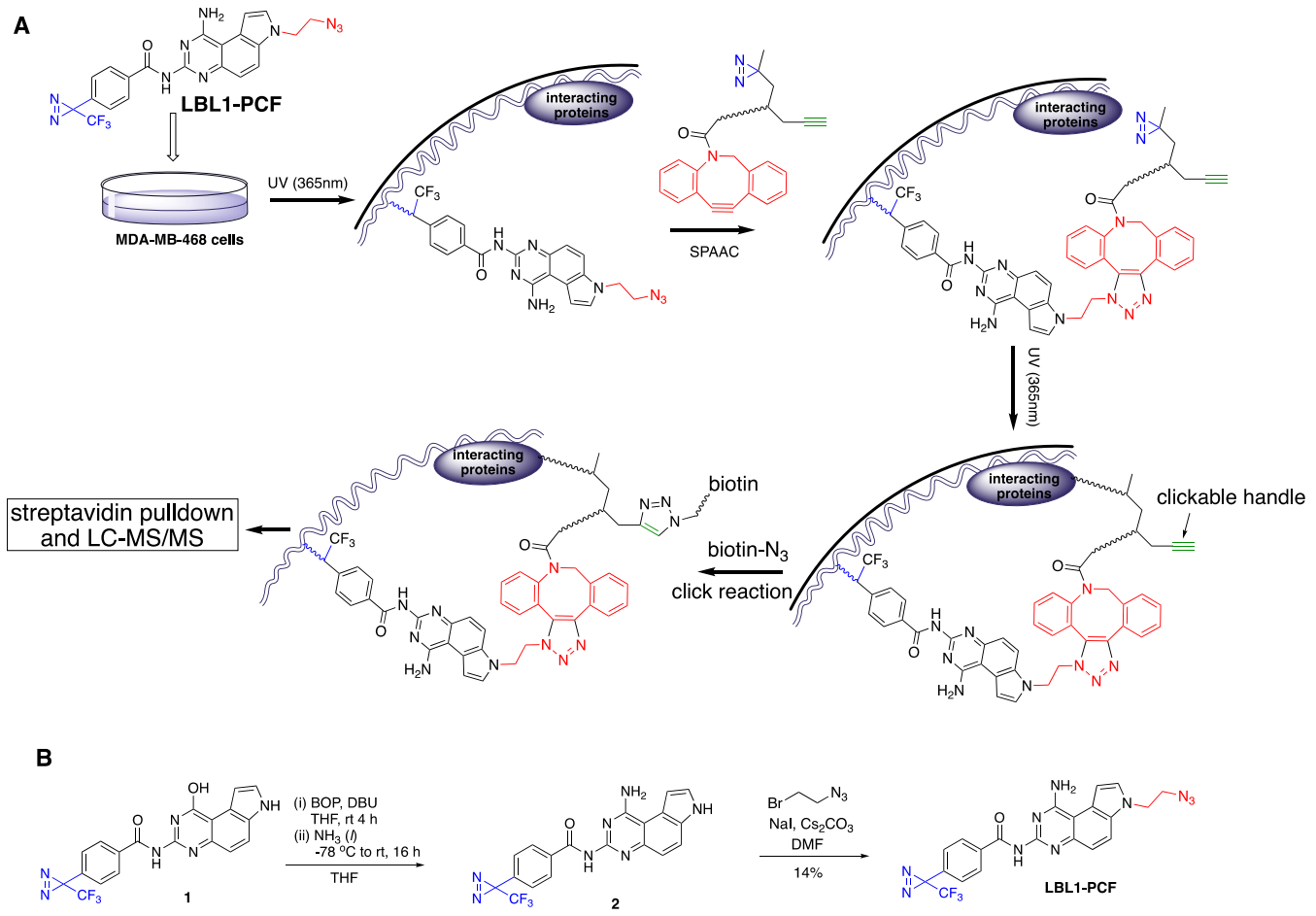

Figure 1. Design of SMAP3-ID to identify lamin interactors in live cells. (A) Schematic flow of SMAP3-ID for identification of lamin interactors in living cells without genetic engineering. (B) Chemical synthesis of **LBL1-PCF**.

lipodystrophy, muscular dystrophy, and premature aging syndrome.[14−16]

Lamins share characteristics consistent with those of other cytosolic IF proteins. They contain a central long α-helical coiled-coil rod domain that is flanked by non-α-helical *N*-terminal head and *C*-terminal immunoglobulin domain tail.[6] No known enzymatic activities have been identified for lamins. Their roles in different biological processes are mediated by different protein−protein interactions. Therefore, identification of proteins that interact with lamins is critical to understand their physiological functions, and such understanding will in turn provide critical insights on how different mutations in *LMNA* can contribute to the various disease etiologies. In pursuit of this goal, different approaches have been developed and utilized to identify such protein−protein interactions.[17] The utility of conventional coimmunoprecipitation (Co-IP) is very limited due to the poor solubility of lamins in physiologically relevant buffers.[18,19] Other approaches have attempted to identify the lamin-binding proteins. These include BioID,[20] OneSTrEP-tag,[21,22] Y2H,[23] Lamin A/C tail,[24] FACS+Salt,[25] biotinylation by antibody recognition (BAR),[26] and more recently APEX2-based proximity labeling.[27] However, all of these methods require overexpression of fusion proteins or cell fixation/permeabilization to identify the binding proteins, rendering them prone to different artifacts. In this paper, we introduce SMAP3-ID (small-molecule-assisted identification of protein−protein interactions through proximity) to identify lamin interactors in native cells under endogenous conditions without genetic manipulation or cell fixation/permeabilization. This approach has the potential to be generalized to interrogate other PPIs in native cells.

RESULTS

Design of LBL1-PCF for SMAP3-ID

Our design of SMAP3-ID (Figure 1A) requires a clickable photoaffinity probe that can undergo a click reaction in live cells. We recently described the identification of **LBL1** (Figure S1) as a specific small molecule to bind lamins in living cells.[13,28] The target identification and engagement of **LBL1** in the cells were assessed and enabled by a clickable photoaffinity probe **LBL1-P** containing a photoaffinity diazirine unit and a clickable terminal alkyne handle (Figure S1). While **LBL1-P** was excellent for target engagement and identification, it is not suitable for live cells due to the incorporated probe alkyne that requires cytotoxic Cu(I) for bioorthogonal click reactions with a tagged azide.[29] To address this issue, we designed **LBL1-PCF** (Figure 1A) with a clickable azide. We envisioned that **LBL1-PCF** will be first photo-cross-linked with lamins in living cells. The bioorthogonal azide group will then undergo a strain-promoted azide−alkyne cycloaddition (SPAAC)[29] with a trifunctional dibenzocyclooctyne (DBCO) probe in live cells. This DBCO derivative contains another diazirine unit and a clickable terminal alkyne. To capture the proteins that interact

https://doi.org/10.1021/jacsau.4c00988
JACS Au 2025, 5, 302−319

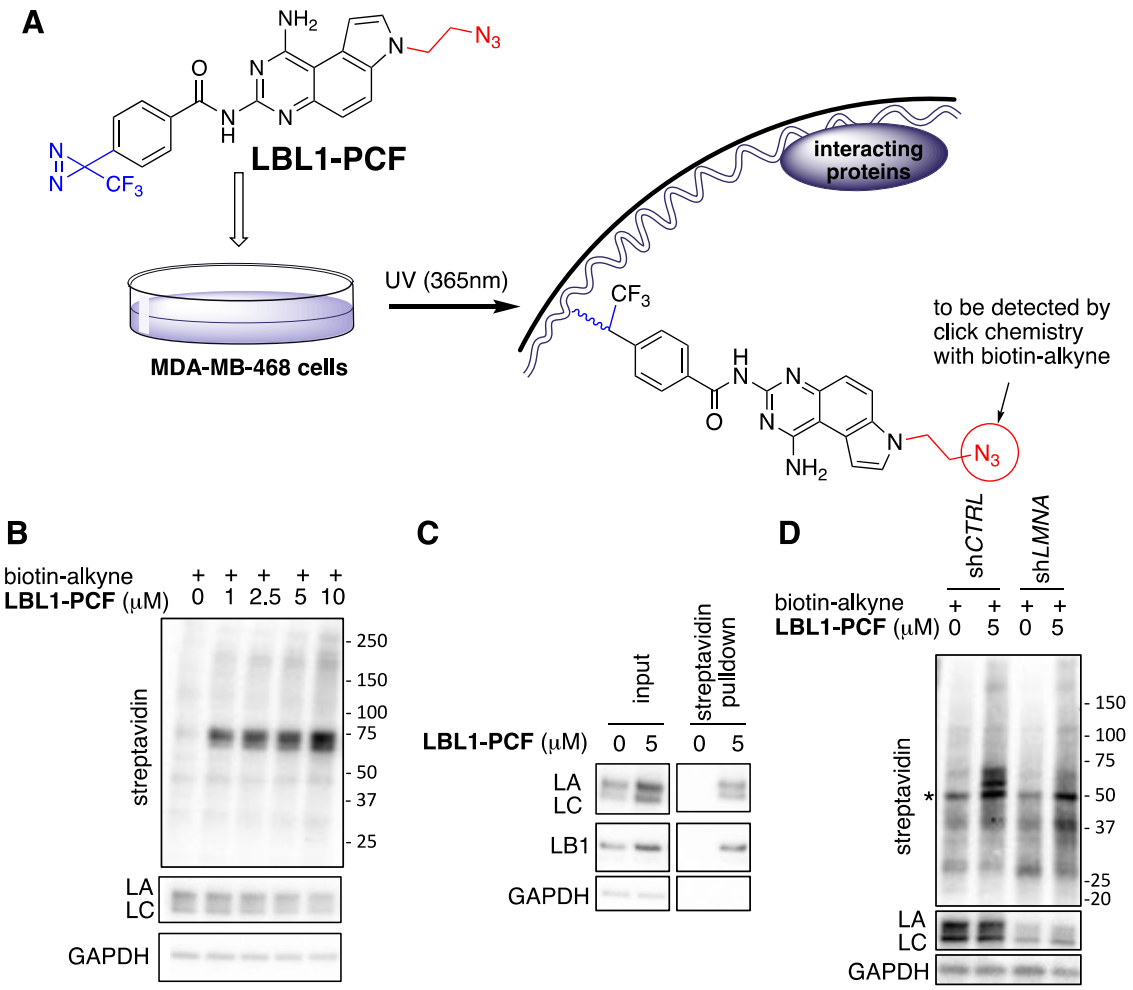

Figure 2. LBL1-PCF targets nuclear lamins. (A) Schematics of **LBL1-PCF** labeling of lamins in cells and its detection strategy. (B) MDA-MB-468 cells were incubated with increasing concentrations of **LBL1-PCF**. Then, the cells were irradiated at 365 nm for 3 min. The whole cell lysates were prepared for a click reaction (CuAAC) with a biotin-alkyne. Then, the clicked lysates were analyzed by SDS-PAGE followed by streptavidin-HRP blotting. Loading for each lane was assessed by Western blotting for LA/LC and GAPDH. (C) The cells were treated as in (B) for the biotin-alkyne click reaction. The clicked cell lysates were subjected to pulldown using streptavidin agarose beads. The bound proteins were eluted from the beads and separated by SDS-PAGE. The membrane was probed with the indicated antibodies. (D) **LBL1-PCF** selectively targets lamins. MEFs with sh*CTRL* or sh*LMNA* were incubated with DMSO or **LBL1-PCF** (5 μM) followed by photo-cross-linking. The lysates were then clicked with a biotin-alkyne. The clicked lysates were then analyzed by SDS-PAGE followed by streptavidin blot. The membrane was also assessed for LA knocking down efficiency. GAPDH was used as a loading control. * indicates a background band present in the MEFs.

with lamins, the diazirine moiety in the trifunctional DBCO compound will be exploited to initiate another covalent cross-linking reaction. At this point, the lamin-interacting proteins are covalently linked to lamins (Figure 1A). To identify the lamin interactors, the remaining clickable terminal alkyne group in the trifunctional DBCO probe can be clicked with biotin-N_3 followed by streptavidin pulldown and mass spectrometry analyses for protein identification (Figure 1A). Due to its small size and longer wavelength for activation, diazirine was chosen as the photo-cross-linker in both **LBL1-PCF** and trifunctional DBCO.

The preparation of **LBL1-PCF** probe is shown in Figure 1B. During our previous synthesis of **LBL1-P**, the alkyne group was installed before the diazirine unit.[28] It was anticipated that direct exchange of the propargyl group for the clickable azide would result in less stable intermediates. Therefore, azido alkylation was reserved for the final synthetic step. Compound **1** was prepared essentially as previously reported.[28] For the next step to regenerate *N*-1 amine via BOP-mediated S_NAr reaction, we found that the yield of this step was significantly improved with liquid ammonia in THF instead of NH_3/MeOH in DMF. The improved yield for compound **2** allowed us to obtain a sufficient amount of material for the next alkylation reaction at the *N*-7 position with bromoethyl azide to provide **LBL1-PCF**. This last step of alkylation typically gave a low yield (14%) of pure product.

LBL1-PCF Targets Nuclear Lamins

With **LBL1-PCF** in hand, we first investigated its suitability for labeling lamins in living cells (Figure 2A). To this end, MDA-MB-468 cells were treated with different concentrations of **LBL1-PCF** followed by UV irradiation at 365 nm. The resulting cell lysates were then reacted with a biotin-alkyne (Figure S1) under Cu(I)-mediated azide alkyne cycloaddition (CuAAC, aka click reaction) using TBTA, TCEP, and $CuSO_4$.[30] The clicked lysates were then separated on an SDS-PAGE gel, and the resulting biotinylated proteins were detected by horseradish peroxidase (HRP)-conjugated streptavidin. We found that **LBL1-PCF** was able to dose-dependently

https://doi.org/10.1021/jacsau.4c00988
JACS Au 2025, 5, 302−319

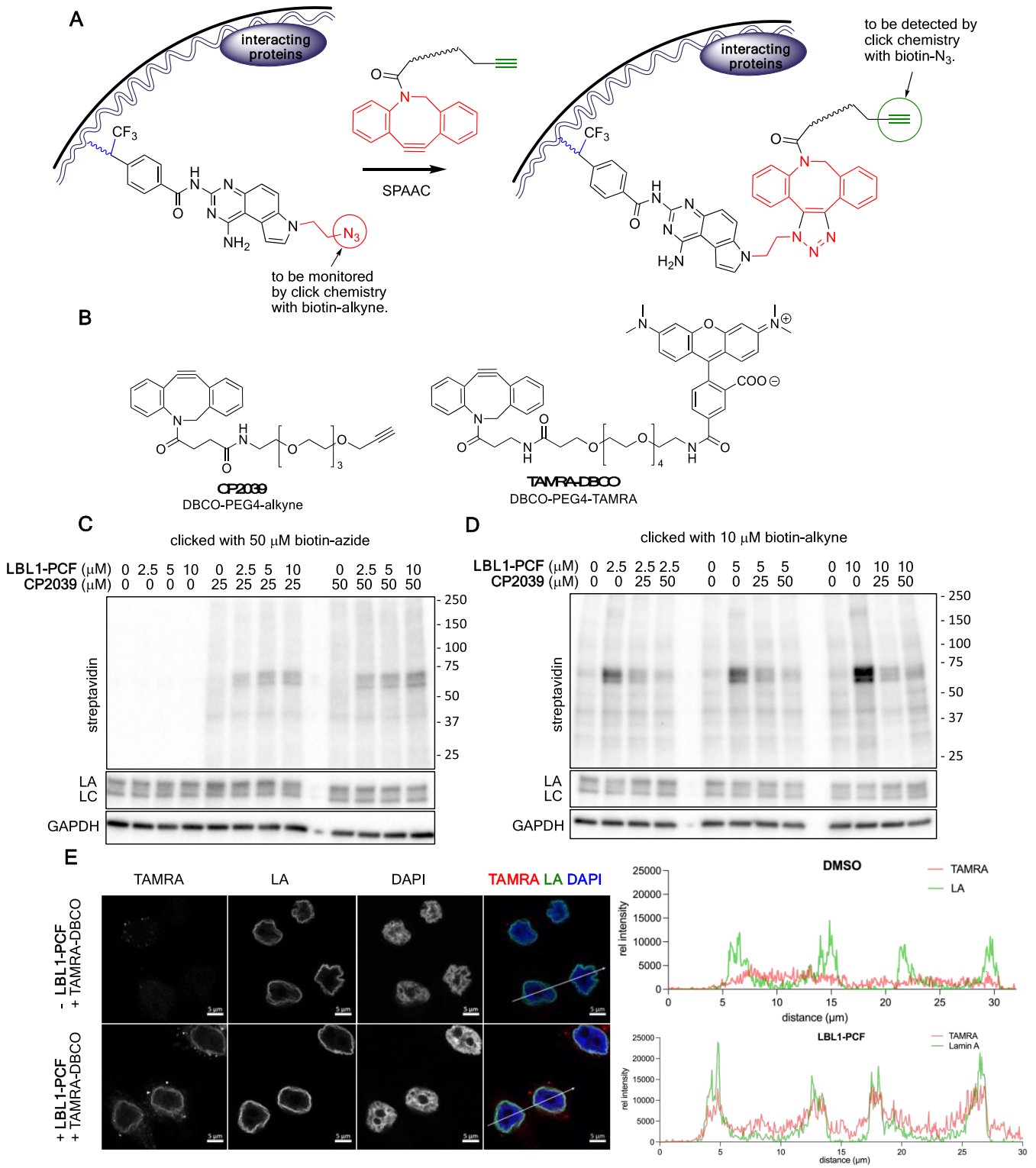

Figure 3. LBL1-PCF undergoes SPAAC in live cells. (A) Schematics for SPAAC in live cells and strategies to detect the azide conjugates and alkyne conjugates using click chemistry. (B) Structures of DBCO-derivatives to be used. (C) MDA-MB-468 cells were first incubated with different concentrations of **LBL1-PCF** followed by UV irradiation. Then, the cells were treated with different concentrations of **CP2039** for 2 h. The cells were collected, and the prepared cell lysates were clicked with biotin-azide (C) or biotin-alkyne (D). The clicked lysates were separated by SDS-PAGE followed by streptavidin blotting. Loading was assessed by Western blot for LA/LC and GAPDH. (E) MDA-MB-468 cells were first treated with **LBL1-PCF** (5 μM) for photo-cross-linking. Then, the cells were treated with **TAMRA-DBCO** (10 μM) for 2 h. The cells were then fixed, permeabilized, and subjected to immunofluorescent labeling with anti-LA. The fluorescence intensity profiles of TAMRA and anti-LA along the indicated lines are presented on the right.

and selectively label 3 bands between 60 and 75 kDa (Figure 2B), which are characteristic of nuclear lamins.[28] When another biotin-alkyne, biotin-dde-alkyne (Figure S1) was used, similar results were obtained (Figure S2). To confirm

https://doi.org/10.1021/jacsau.4c00988
JACS Au 2025, 5, 302−319

Scheme 1. Synthesis of Trifunctional DDZ3

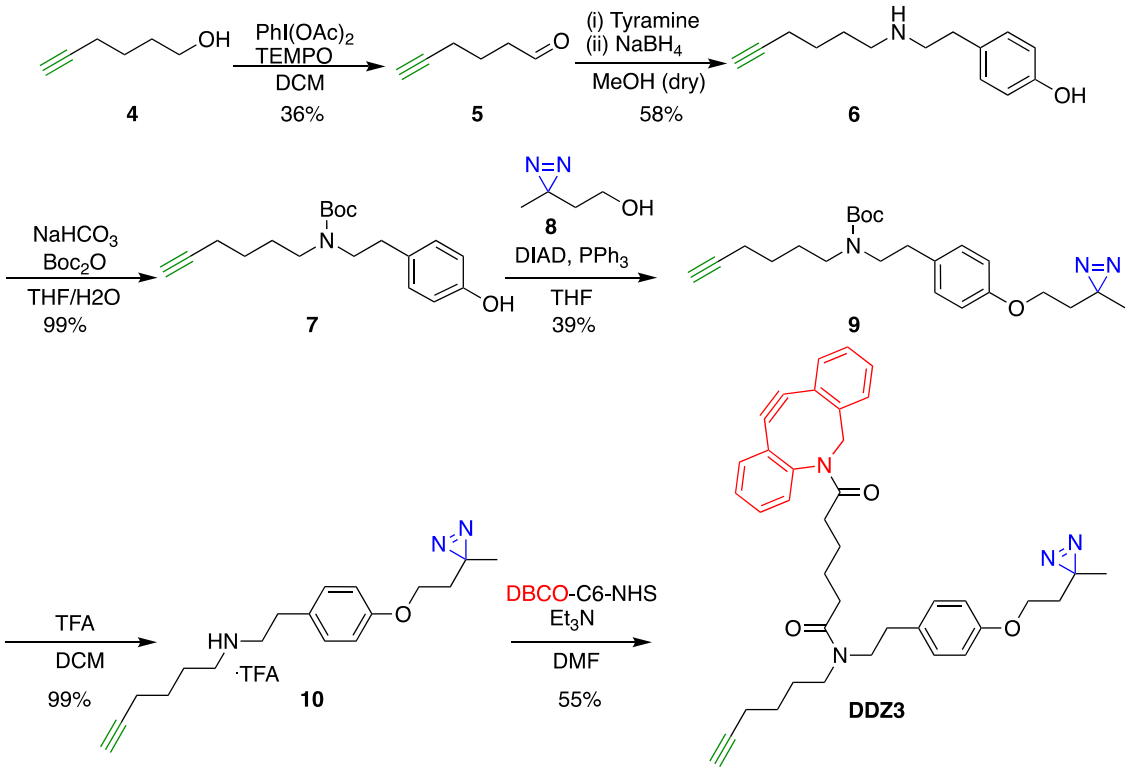

that lamins were indeed labeled by **LBL1-PCF**, the biotin-alkyne clicked lysates were subjected to streptavidin agarose precipitation, and the bound proteins were analyzed by Western blot using antibodies for LA and LB1. As shown in Figure 2C, LA and LB1 were efficiently pulled down when **LBL1-PCF** was incubated with the cells. As a negative control, GAPDH was not present in the streptavidin pulldowns, demonstrating the specificity of **LBL1-PCF**. To investigate the labeling specificity of **LBL1-PCF** in the entire cellular proteome, the aforementioned streptavidin-bound proteins were analyzed by LC-MS/MS. Indeed, we observed that LA and LB1 were highly enriched by **LBL1-PCF** (Table S1 and Figure S3), a result similar to what we obtained previously with **LBL1-P**.[28]

To further confirm the selectivity and specificity, we evaluated **LBL1-PCF**'s labeling using mouse embryonic fibroblasts (MEF) that lack B-type lamins. These MEFs were derived from *LMNB1* and *LMNB2* double-knockout mouse embryos.[31] **LBL1-PCF** labeled LA efficiently in these MEFs (sh*CTRL*) (Figure 2D). The remaining *LMNA* in the MEFs was further knocked down using sh*RNA* as we previously described.[13] As shown in Figure 2D, LA was efficiently knocked down in the MEFs using sh*LMNA*. When LA was knocked down in these MEFs, the labeling by **LBL1-PCF** was significantly attenuated (Figure 2D). These results demonstrate that **LBL1-PCF** can specifically label lamins in living cells and can therefore be further investigated as an appropriate probe for SMAP3-ID in living cells.

LBL1-PCF Undergoes SPAAC in Living Cells

With the lamin-binding specificity of **LBL1-PCF** established in living cells, we next investigated the possibility of the azide functional group in **LBL1-PCF** to undergo SPAAC with a DBCO functional group in living cells (Figure 3A). As an initial test, we chose the commercially available bifunctional DBCO-containing alkyne **CP2039** (Figure 3B) as the reaction partner with the azide in **LBL1-PCF**. It was anticipated that a successful SPAAC in live cells would consume the azide in **LBL1-PCF** already conjugated to lamins to generate lamins labeled with an alkyne from **CP2039**. MDA-MB-468 cells were first treated with **LBL1-PCF** followed by UV irradiation at 365 nm. Then, the cells were incubated with **CP2039** for *in cellulo* SPAAC. The resulting crude cell lysates were then clicked with a biotin-azide (Figure S1) to label **LBL1-PCF−CP2039** conjugates for streptavidin blot analysis. As shown in Figure 3C, strong and dose-dependent biotinylated lamin signals were observed with a combination of **LBL1-PCF** and **CP2039**. As expected, the biotin-N_3 clickable signal was not observed when **CP2039** was omitted from the treatment protocol (Figure 3C, left 4 lanes). The bioorthogonality of the alkyne and azide functional groups also allowed us to investigate the extent of SPAAC reaction completion in living cells. As shown in Figure 3D, when MDA-MB-468 cells were treated with different combinations of **LBL1-PCF** and **CP2039** and the cell lysates were subjected to click reactions with a biotin-alkyne (Figure S1), we observed a dose-dependent reduction of biotinylated lamin signals, indicating consumption of azide group in **LBL1-PCF** by **CP2039**. Almost complete consumption of azide was achieved with 50 μM **CP2039** (Figure 3D).

The SPAAC of **LBL1-PCF** in living cells was further assessed using fluorescence microscopy to examine its subcellular localization. MDA-MB-468 cells were first incubated with **LBL1-PCF** (5 μM). Then, the cells were treated with fluorescent SPAAC-capable rhodamine derivative **TAMRA-DBCO** (Figure 3B). The cells were then fixed, permeabilized, and coimmunostained with anti-LA. As shown in Figure 3E (bottom panel), when the cells were treated with **LBL1-PCF**, a strong TAMRA signal was observed. The observed TAMRA signal colocalized very well with anti-LA

https://doi.org/10.1021/jacsau.4c00988
JACS Au 2025, 5, 302−319

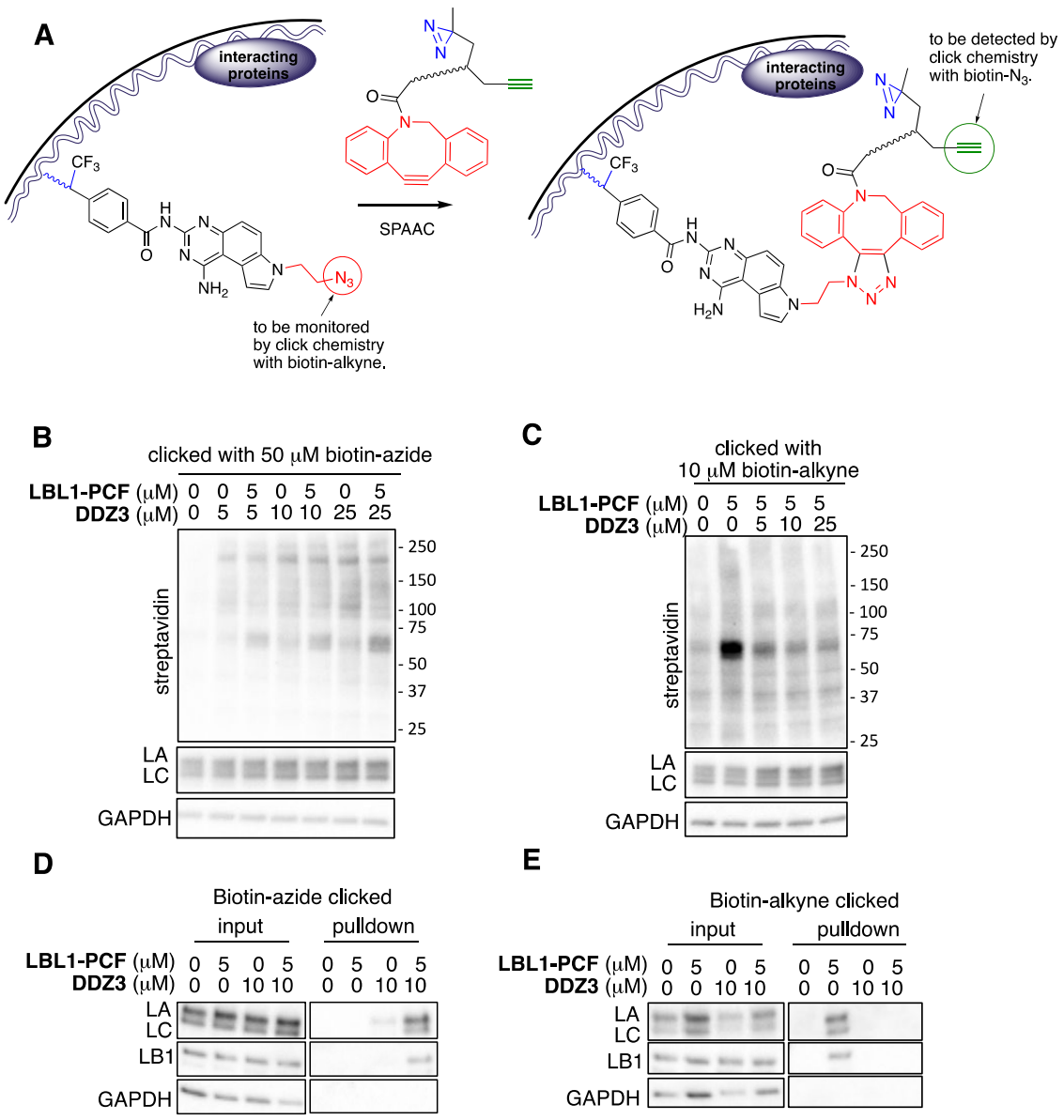

Figure 4. LBL1-PCF reaction with **DDZ3** to label lamins in native cells. (A) Schematics for SPAAC with **DDZ3** in live cells and strategies to detect the azide conjugates and alkyne conjugates using click chemistry. (B, C) MDA-MB-468 cells were first incubated with **LBL1-PCF** for photo-cross-linking. The cells were further incubated with different concentrations of **DDZ3** for 2 h. Then, the cells were harvested, and the resulting whole cell lysates were clicked with biotin-azide (B) or biotin-alkyne (C). The clicked lysates were separated on an SDS-PAGE gel followed by streptavidin blotting and Western blotting with indicated antibodies. (D, E) Conjugation of lamins to **DDZ3** through **LBL1-PCF**. MDA-MB-468 cells were treated as indicated. The biotin-azide (D) or biotin-alkyne (E) clicked lysates were then subjected to pull-down using streptavidin agarose. After extensive washing, the bound proteins were analyzed with indicated antibodies.

signal. This colocalization further demonstrated that **LBL1-PCF** labeled lamins in living cells, similar to previously described **LBL1-P**.[28] No significant TAMRA signal was observed in the cells without treatment with **LBL1-PCF** (Figure 3E, top panel). Altogether, these results demonstrated that **LBL1-PCF** was able to selectively label lamins and undergo SPAAC in live cells.

Design and Evaluation of a Trifunctional DBCO Probe DDZ3

Having established that **LBL1-PCF** can label lamins and undergo SPAAC in living cells, we sought to develop an appropriate trifunctional DBCO probe for our designed SMAP3-ID approach (Figure 1A). We designed **DDZ3** for this purpose (Scheme 1). Specifically, **DDZ3** contains three essential functional groups: a DBCO unit to undergo SPAAC, a diazirine unit to covalently capture LA-interacting proteins, and a terminal alkyne for another CuAAC reaction to enrich the captured proteins. The synthesis of **DDZ3** is shown in Scheme 1. 5-Hexynol (**4**) was first oxidized to its corresponding aldehyde **5**. A reductive amination between tyramine and aldehyde **5** provided amine **6**, which was then protected with Boc_2O to give the Boc-protected compound **7**. The diazirine moiety was installed using a Mitsunobu reaction between diazirine alcohol **8**, prepared according to our previously optimized protocol,[32] and phenol compound **7** to yield **9**. The Boc group in **9** was deprotected to provide amine **10**. Finally, the acylation of amine **10** with a commercially available DBCO-C6-NHS ester furnished the desired **DDZ3**.

https://doi.org/10.1021/jacsau.4c00988
JACS Au 2025, 5, 302−319

With **DDZ3** in hand, we evaluated its specific reactivity with **LBL1-PCF** in live cells (Figure 4A). Similar to **CP2039**, the SPAAC product with **DDZ3** would retain the terminal alkyne that could be detected using click chemistry with a biotin-N_3. To this end, MDA-MB-468 cells were treated with **LBL1-PCF** followed by UV irradiation (365 nm). Then, the cells were incubated with different concentrations of **DDZ3**. The cells were then harvested, lysed, and clicked with a biotin-N_3 to assess the generated **LBL1-PCF-DDZ3** conjugates. The clicked lysates were then separated with SDS-PAGE followed by streptavidin blotting. As shown in Figure 4B, the signals generated by the dual treatment of **LBL1-PCF** and **DDZ3** were dose-dependent and consistent with the labeling of the lamins. These results are also similar to the ones shown in Figure 3C with another DBCO compound, **CP2039**, albeit the background labeling by **DDZ3** was somewhat higher than that of **CP2039**. This background labeling was likely due to the nonspecific reactivity of the DBCO unit with protein thiols in the cells to generate covalently protein-bound **DDZ3**.[33] Similar results were obtained when the cell lysates were clicked with a biotin-dde-azide (Figure S4B). Consumption of the azide in **LBL1-PCF** by **DDZ3** was also assessed by a Cu(I)-mediated click with a biotin alkyne. The intensity of the biotinylated signals decreased with increasing concentrations of **DDZ3** (Figure 4C). Similar results were obtained when these lysates were clicked with a biotin-dde-alkyne to confirm the consumption of azide (Figure S4C). To further confirm that lamins were indeed enriched by the combination of **LBL1-PCF** and **DDZ3**, the treated and clicked cell lysates were subjected to streptavidin agarose precipitation, and the bound proteins were analyzed using Western blot analyses. As shown in Figure 4D, LA and LB1 were efficiently pulled down from the streptavidin agarose precipitation. As a negative control, GAPDH was not present in the pulldown. Importantly, if the cell lysates from the cells treated with **LBL1-PCF** and **DDZ3** were clicked with a biotin-alkyne to evaluate the SPAAC reaction completion, we found that LA and LB1 were efficiently and specifically pulled down with streptavidin agarose beads only when **DDZ3** was omitted from **LBL1-PCF**-treated cells (Figure 4E). Altogether, these results demonstrated that the combination of **LBL1-PCF** and **DDZ3** can potentially be used for SMAP3-ID to identify lamin-interacting proteins in native cells.

Identification of Lamin Interactors by SMAP3-ID with the Combination of LBL1-PCF and DDZ3 in Native Cells

With both **LBL1-PCF** and **DDZ3** validated for lamin binding and SPAAC in living cells, respectively, we next turned our attention to identify the lamin interactors from living cells in the endogenous setting via sequential exploitation of the diazirine unit and terminal alkyne present in **DDZ3** (Figure S5A). The feasibility of the combination of **LBL1-PCF** and **DDZ3** for further photo-cross-linking was first investigated by streptavidin blotting. It was anticipated that treatment of the cells with **LBL1-PCF** and **DDZ3** followed by a second round of photo-cross-linking would initiate cross-linking between lamins and their binding proteins (Figure S5A). This would generate cross-linked species consisting of lamins and their binding partners. As shown in Figure S5B and consistent with the results in Figure 4B, when the cell lysates from the cells treated with **LBL1-PCF** and **DDZ3** were clicked with a biotin-N_3, the lamin signals were prominent in the streptavidin blot. If the cells were subjected to a second round of UV irradiation after treatment with **DDZ3**, the apparent signals for parental lamins (60−75 kDa) were decreased. On the other hand, there was a concomitant increase of streptavidin signals at the higher-molecular-weight region, which are consistent with the potential cross-links between lamins and their binding proteins that are now tagged with a biotin.

To identify the proteins that would interact with lamins using SMAP3-ID (Figure S5A), MDA-MB-468 cells were treated with **LBL1-PCF** followed by photo-cross-linking. Then, the cells were treated with **DDZ3** to initiate SPAAC inside the living cells. Upon removing excess unreacted **DDZ3**, the cells were again UV-irradiated to initiate photo-cross-linking with lamin-binding proteins. Then, the cells were lysed and clicked with biotin-N_3 for streptavidin agarose precipitation. The bound proteins were eluted, and their identities were analyzed by LC-MS/MS. The relative abundance of each protein was quantified by label-free spectra counting (Table S2). This analysis identified 1150 proteins that have at least one spectra count more than the vehicle-treated sample (Table S2). Further comparison between the dual probe-treated sample (**LBL1-PCF** and **DDZ3**) and the **DDZ3** alone-treated sample provided 417 proteins that were selectively enriched in the dual probe-treated sample. This list of 417 proteins represents potential lamin interactors in native MDA-MB-468 cells (Table S2). Among these proteins are known lamin-interacting proteins and those that reside in the nuclear envelope. Examples of these hits include LA, LB1, LAP2a, Nup93, RAN, Nup43, ICMT, FACE1/ZMPSTE24 and HP1. Gene Ontology (GO) analysis of the 417 proteins using g:Profiler[34] identified many molecular functions and biological processes that are significantly enriched (Table S3). Selected enriched GO terms for biological pathways and molecular functions are shown in Figure S5C and S5D, respectively. Consistent with the known roles of lamins, many enriched proteins are involved in protein binding (e.g., LA, LB1, HNRNPU, CBX3), chromatin binding (e.g., HNRNPU, NPM, CBX3, RUVB2), protein localization (e.g., LA, LB1, NPM, Nup93, RAN), and nucleocytoplasmic transport (e.g., LA, NPM, Nup93, Nup46). Interestingly, the GO terms for RNA metabolism, tricarboxylic acid cycle (TCA), and oxidoreductase activity are among the most significantly enriched terms (Figure S5C and S5D), suggesting that lamins may interact with these proteins to regulate RNA metabolism and cellular metabolic activities.

Given the diversity of proteins identified to interact with lamins through SMAP3-ID, we interrogated this list of proteins with the lamina-omes identified using other methods (Table S4). As shown in the Venn diagrams in Figure S6 and Table S4, the overlaps between the proteins varied among the methods. The highest overlap was observed between SMAP3-ID and APEX2 while the lowest was observed between SMAP3-ID and Y2H. The wide range of differences in overlap was also observed when the lamina-ome obtained from BAR was compared with those obtained by other methods.[26] These differences likely arise from the approaches to be used, as well as the cell types to be employed in each experiment. Therefore, validation of the identified hits will be critical in each scenario.

Validation of Identified Lamin-Interacting Proteins

A number of known and unknown lamin-binding proteins enriched by the treatment of **LBL1-PCF** and **DDZ3** were selected for independent validation using co-IP and confocal microscopy assays. We first evaluated the candidates by co-IP

https://doi.org/10.1021/jacsau.4c00988
JACS Au 2025, 5, 302−319

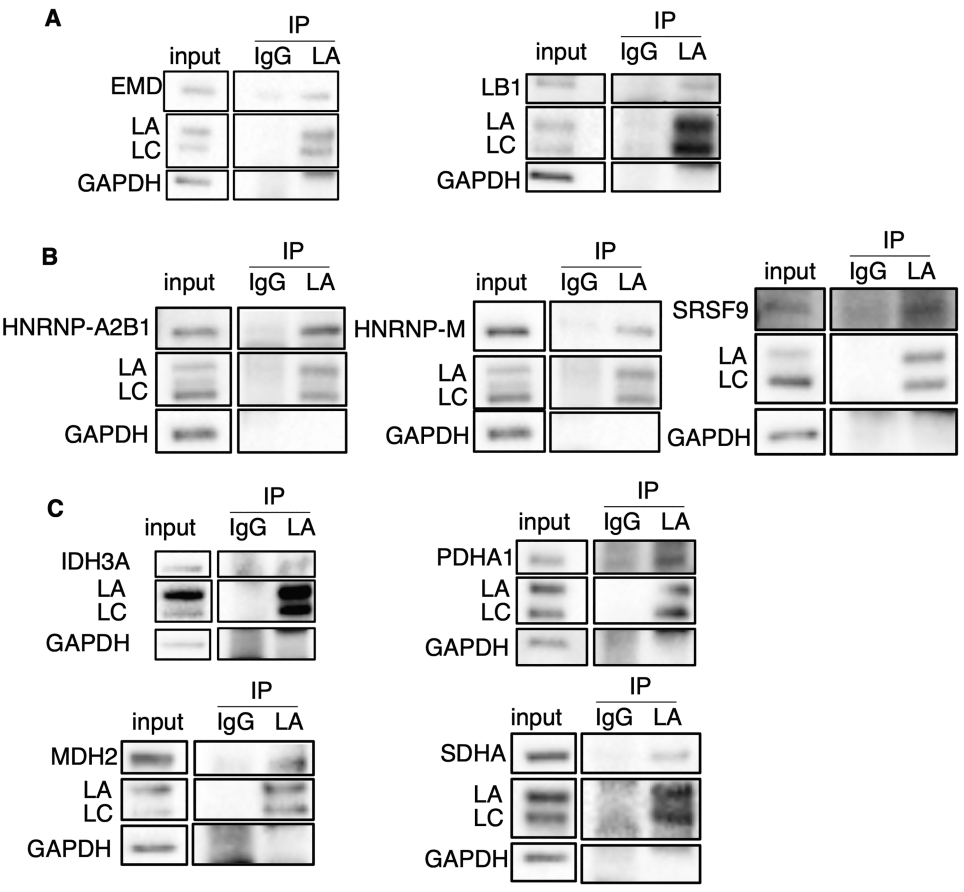

Figure 5. Validation of identified lamin interactors with LA by co-IP. MDA-MB-468 cells were collected, and the lysates were prepared for co-IP with IgG (mouse) or anti-LA (mouse) as described in the Experimental Section. The bound proteins were eluted and analyzed by Western blot with indicated antibodies ((A) known LA-binding partners; (B) RNA-binding proteins; (C) metabolic enzymes). GAPDH was used as a negative control.

using LA as the bait. EMD and LB1 were chosen as the positive controls.[35,36] As mentioned previously, lamins are not very soluble in physiologically relevant buffers. Inclusion of nonionic detergent Nonidet P-40 helped extract lamins, although a substantial amount of lamins remained insoluble (Figure S7). As shown in Figure 5A, both EMD and LB1 were detected in the anti-LA immune complex from the MDA-MB-468 cells. Given the prominent enrichment of proteins involved in RNA metabolism, the TCA cycle, and oxidoreductase activity (Figure S5C and S5D), we further validated some of these less well-characterized candidates to interact with lamins. Previous proximity labeling using LB1-APEX2 found that LB1 was also involved in binding with RNA and RNA-metabolizing proteins.[27] We selected heterogeneous nuclear ribonucleoproteins HNRNP-A2B1 (ROA1), HNRNP-M and splicing factor SRSF9 for further validation. As shown in Figure 5B, all of these three RNA-binding proteins were found to be present in the anti-LA immune complex. Different efficiencies were observed for these co-IP results, suggesting that they show differential binding affinities with LA under our conditions of co-IP. The proteins from the groups belonging to the metabolic processes for ATP generation selected for co-IP validation were IDH3A, MDH2 (MDHM), PDHA1 (ODPA), and SDHA, which are all nuclear-encoded enzymes. As shown in Figure 5C, we observed binding for all of the four metabolic enzymes with LA using the co-IP assay. Similar to the RNA-binding proteins evaluated, the efficiency of co-IP varied across the different proteins, potentially reflecting different binding affinities under these conditions.

The interaction between LA and RNA-binding proteins or metabolic enzymes was further assessed using confocal microscopy to evaluate their colocalization in the cells. To this end, MDA-MB-468 cells were fixed and permeabilized for staining with anti-LA and indicated RNA-binding proteins or metabolic enzymes. As expected, LA was predominantly localized at the nuclear rim as well as inside nucleoplasm (Figure 6A). All three RNA-binding proteins (HNRNP-A2B1, HNRNP-M, and SRSF9) were localized inside the nucleus with a differential staining pattern (Figure 6A). However, upon careful examination of the staining patterns, both LA and the RNA-binding proteins were found to be present on the inner side of the nuclear rim (see Figure 6A, zoom-in region and their corresponding fluorescence intensity profiles on the right), supporting the co-IP results shown in Figure 5B that these proteins interact with each other in the cells.

The mitochondrial metabolic enzymes were similarly evaluated for their localization patterns in cells along with LA. We first evaluated if the four metabolic enzymes (IDH3A, MDH2, PDHA1, and SDHA) were localized in mitochondria in MDA-MB-468 cells. To test this, the cells were stained with mitochondrial dye MitoView640 along with individual antibodies. As expected, all of the four enzymes are localized in mitochondria (Figure S8). However, the mitochondrial localization of these enzymes was not exclusive, and some

https://doi.org/10.1021/jacsau.4c00988
JACS Au 2025, 5, 302−319

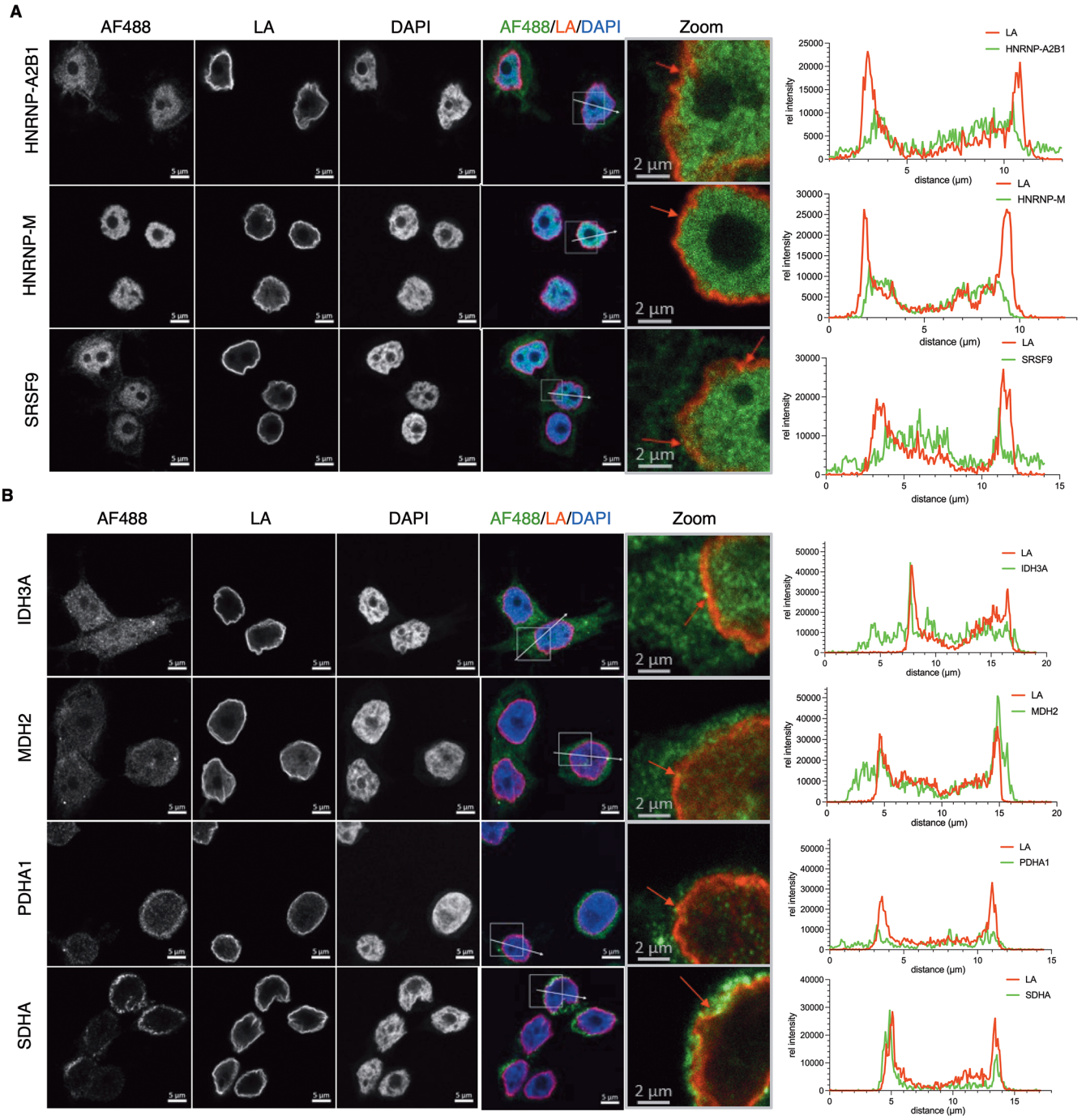

Figure 6. Localization of RNA-binding proteins and metabolic enzymes in MDA-MB-468 cells. MDA-MB-468 cells were fixed, permeabilized, and stained with indicated antibodies for RNA-binding proteins (A) or mitochondrial metabolic enzymes (B) along with anti-LA. Then, the cells were further incubated with fluorescently labeled secondary antibodies for confocal microscopy. Representative micrographs are shown. The zoomed-in view of the boxed regions is presented with red arrows indicating where the two proteins were juxtaposed. The fluorescence intensity profiles of LA and indicated proteins along the white arrows are shown on the right side of each panel. Scale bars are either 5 or 2 μm.

nuclear localization was also observed. Nuclear localization of these enzymes was previously reported in other cell types.[37] To investigate if these enzymes in the nucleus and LA can interact with each other in the cells, we co-stained the cells with anti-LA. As shown in Figure 6B, a fraction of these mitochondrial metabolic enzymes was found to be associated with LA either at the nuclear lamina or in nucleoplasm, where LA is localized. The interactions of these enzymes with LA are better represented in reconstituted 3D images of the cells with or without a mask of the nucleus, as shown in Figure S9. Altogether, our co-IP and confocal microscopy results support that LA interacts with both RNA-binding proteins and mitochondrial enzymes involved in glycolysis and the TCA cycle.

LBL1 Modulates Mitochondrial Activities

Given the direct interactions between LA and mitochondrial metabolic enzymes we identified, we were intrigued to investigate whether a small-molecule lamin inhibitor **LBL1**[13]

https://doi.org/10.1021/jacsau.4c00988
JACS Au 2025, 5, 302−319

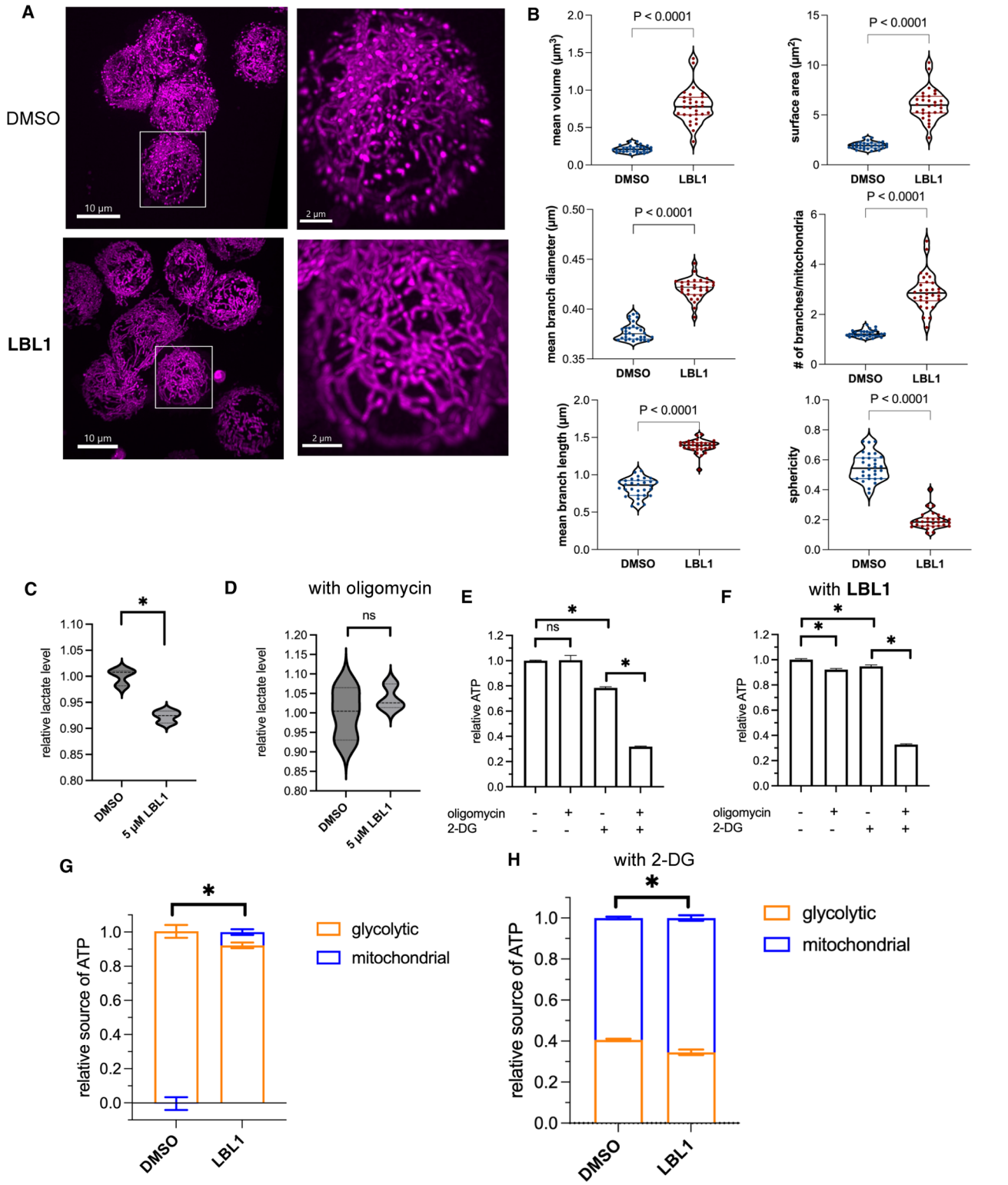

Figure 7. LBL1 modulates mitochondrial networks and activities. (A) MDA-MB-468 cells were treated with DMSO or **LBL1** (5 μM) for 18 h. Then, the mitochondria were labeled with MitoView640 and the mitochondria were examined under a microscope by live cell imaging. Representative mitochondrial networks and zoomed-in views are presented. (B) The mitochondria shown in (A) were analyzed using Mitochondrial Analyzer, and the parameters are presented along with their *P* values. For each violin plot, the median and quartile lines are shown. The data were from 30 random regions of interest (ROI) under each condition. Each ROI had 10−20 cells. (C−D) MDA-MB-468 cells were treated with **LBL1** as indicated for 18 h. Then, the cells were switched to FBS-free medium and further treated with (D) or without (C) oligomycin for 2 h. The lactate concentration in the cell culture media was measured using Lactate-Glo assay. The lactate concentration was normalized to the cell number in each well. (E, F) MDA-MB-468 cells were treated with **LBL1** as indicated for 18 h. Then, oligomycin and 2-DG were added as indicated for 2 h. The cellular ATP level was measured using the CellTiter-Glo assay and normalized to the protein concentration. (G−H) The data in (E) and (F) were converted into cellular bioenergetic organization as detailed in the Experimental Section. * indicates $P < 0.05$. The *P* values were from the Student's *t*-test.

https://doi.org/10.1021/jacsau.4c00988
JACS Au 2025, 5, 302−319

might modulate the cellular mitochondrial functions. Previous studies have shown that different LA mutants could affect mitochondrial morphology and bioenergetics,[38−40] but the mechanisms were not clear. We treated MDA-MB-468 cells with **LBL1** (5 μM) and then the mitochondria were labeled with a mitochondrial dye MitoView640 in live cells. The morphologies of the mitochondria were examined by using live cell imaging. As shown in Figure 7A, the mitochondria networks in the cells treated with **LBL1** appeared to be morphologically more complex than those from vehicle-treated cells. To quantitatively analyze the differences between the two populations of mitochondria, we employed Mitochondria Analyzer[41] in ImageJ to analyze the 3D stacks of the cells. There was a significant increase in the mean volume and mean surface area of the mitochondria from the cells treated with **LBL1** (Figure 7B). The branch diameter, number of branches, as well as the mean branch length were also increased with **LBL1** treatment. The sphericity of the mitochondria was decreased with **LBL1** treatment, indicating general mitochondrial elongation (Figure 7B). On a per mitochondrial basis, we also observed an increase of total branch lengths, branch junctions, and number of branch end points from the live mitochondria treated with **LBL1** (Figure S10A−C). These results support the idea that **LBL1** significantly modulates the connectivity of the mitochondrial networks in live cells, potentially reflecting the effect of **LBL1** in modulating the interactions between lamins and mitochondrial proteins identified from our SMAP3-ID studies.

The striking morphological changes of mitochondria induced by **LBL1** suggested that it might modulate the mitochondrial activity as the energy-producing organelle. The cellular ATP is generated from either glycolysis or mitochondrial respiration. During glycolysis, the glucose molecule is metabolized into pyruvate, which is then converted into lactate that can be secreted into extracellular space. To determine whether **LBL1** could modulate glycolysis, we measured the extracellular lactate level. As shown in Figure 7C, **LBL1** treatment resulted in a decrease of lactate level, suggesting that the glycolysis level was inhibited by **LBL1** or **LBL1** might shift the cellular ATP production from glycolysis to mitochondrial respiration. To further test this, we treated cells with oligomycin, which is a mitochondrial ATP synthase inhibitor to inhibit mitochondrial ATP synthesis.[42,43] Inhibition of mitochondrial ATP synthesis resulted in an increase of glycolysis, as evidenced by the increase of lactate level (Figure S10D) to meet the cellular energy demand. When mitochondrial ATP synthesis was inhibited by oligomycin, **LBL1** treatment did not result in a decrease of the cellular glycolysis level (Figure 7D) as measured by the lactate level, indicating that the decrease of glycolysis by **LBL1** in the absence of mitochondrial inhibition was due to a shift of the cellular ATP source from glycolysis to mitochondrial respiration.

To further assess the effect of **LBL1** on the metabolic shift, we investigated the source of ATP generation in the presence of **LBL1** and different metabolic inhibitors. When cells were treated with oligomycin, no significant change in cellular ATP was observed (Figure 7E). This is consistent with earlier reports that triple-negative breast cancer (TNBC) cell lines exhibited a high glycolytic rate and reserve under these conditions.[44,45] Treatment of the cells with a glycolysis inhibitor 2-deoxyglucose (2-DG)[46] resulted in a reduction in cellular ATP and this reduction was further exacerbated when the cells were cotreated with oligomycin (Figure 7E). On the other hand, when the cells were treated with **LBL1** and oligomycin, we observed that the cellular ATP level was decreased compared to the cells not treated with oligomycin (Figure 7F). We calculated the relative contribution of glycolysis and mitochondrial respiration to the total cellular ATP as described before[47] to understand how **LBL1** modulated cellular bioenergetic organization. Consistent with the results shown in Figure 7E, mitochondrial respiration contributed little to the total cellular ATP concentration (Figure 7G) without **LBL1** treatment. However, when the cells were treated with **LBL1**, mitochondrial respiration made a significant contribution to the cellular ATP. The increased mitochondrial respiration to the cellular ATP was present even when the cells were treated with 2-DG (Figure 7H). Altogether, these results suggest that the hyperfused mitochondrial networks induced by **LBL1** in the cells were more active in producing ATP and contributing to the total cellular ATP.

DISCUSSION AND CONCLUSIONS

The identification of subproteomes in a given cellular compartment and protein complex is critical to understand their biological functions and how therapeutics may modulate these subproteomes. As described in the Introduction section, many different methods have been developed to elucidate these subproteomes. In this report, we developed a unique small-molecule-based SMAP3-ID approach to identify endogenous lamin-interacting proteins in native cells based on our previously described **LBL1**. The salient feature of SMAP3-ID is that no genetic engineering or cell fixation/permeabilization is required and therefore it is amenable to identify the protein complexes in native cells. This unique feature provides advantages over other existing approaches to identify lamin-interacting proteins. The keys to this approach are the availability of **LBL1** as a selective lamin-binding ligand,[13] a live cell-compatible bioorthogonal click reaction, and two carefully designed photo-cross-linking reactions to capture the interacting proteins in the native cellular state. Using this strategy, many known LA-interacting proteins were identified, establishing its feasibility. Furthermore, we discovered previously unknown LA-interacting proteins, including RNA-binding proteins and mitochondrial proteins. All of the newly discovered candidate proteins selected for validation (HNRNP-A2B1, HNRNP-M, SRSF9, IDH3A, MDH2, PDHA1, and SDHA) were confirmed to interact with LA by both co-IP and confocal colocalization analyses.

Our discovery that LA interacts with mitochondrial enzymes involved in the TCA cycle is noteworthy since these proteins were anticipated to be localized in two different organelles. Indeed, our data showed that these metabolic enzymes are primarily localized in the mitochondria. However, nuclear localization of these enzymes was also observed to some extent. Others have also recently reported nuclear localization of TCA enzymes in different cell types under different conditions.[37,48−51] The nuclear localized TCA enzymes can potentially regulate the production of TCA cycle intermediates for epigenetic regulation of protein functions (e.g., protein acetylation and succinylation). Our discovery of direct interaction between LA and TCA enzymes may also provide a means for these enzymes to be transported to nucleus from mitochondria as has been shown for pyruvate dehydrogenase complex (PDC).[48] In this regard, it has been reported that mutations or deletion of *LMNA* generate phenotype of

https://doi.org/10.1021/jacsau.4c00988
JACS Au 2025, 5, 302−319

dysfunctional mitochondria with impaired mitochondrial bioenergetics.[38,39,52,53] Although the mechanisms underlying this alteration of mitochondrial activity have not yet been clarified, our discovery that LA directly interacts with the TCA enzymes suggests that mutations in LA can potentially modulate its interactions with these enzymes and thus their activities. For example, the levels of TCA intermediates arising from the competent TCA enzymes in the nucleus may be influenced by their interaction with LA, which can subsequently affect the post-translational modification of proteins.[37,50]

Based on the direct interaction between LA and TCA enzymes, we further investigated the effect of our recently discovered small-molecule lamin-binding ligand **LBL1** on mitochondrial network morphology and bioenergetics. We found that **LBL1** extensively modified the mitochondrial morphology to an elongated, hyperfused phenotype. This change of mitochondrial morphologies likely contributed to the enhanced mitochondrial activity for efficient ATP generation. We previously showed that **LBL1** inhibited homologous recombination repair of DNA double-strand breaks via enhanced degradation of DNA recombinase Rad51.[13] The metabolic shift induced by **LBL1** described here suggests that the compound or its derivatives may also be effective in glycolysis-addicted cancer cells (i.e., Warburg effect).[54]

The major advantage of SMAP3-ID to identify protein−protein interactors is that no genetic engineering or overexpression of target proteins is needed, which enables the investigation of the protein−protein interactions in the native cellular state. Additionally, the size of diazirine unit to be incorporated in the first probe **LBL1-PCF** is small, obviating the potential consequences of changing binding properties compared to the initial ligand **LBL1**. The recently introduced microenvironment mapping (μMap) via Dexter energy transfer using photocatalyst can also potentially identify such subproteomes in native cells although a bulky photocatalyst is needed to be appended to a ligand or antibody,[55,56] which may interfere with the ligand binding in certain cases. However, our SMAP3-ID approach does have certain limitations. One limitation of SMAP3-ID is the potential background labeling by **DDZ3** itself due to protein thiol reactivity with DBCO, which may mask certain true protein−protein interactions. For example, EMD was not in our list of 417 proteins that interact with lamins. This is due to the fact that EMD was abundantly labeled by **DDZ3** alone (Table S2). The other limitation is the availability of highly specific small-molecule ligands to a protein of interest. Many small-molecule inhibitors, including clinically approved drugs, have been developed and can be functionalized for SMAP3-ID studies. Furthermore, the recent developments in chemical genetics and chemoproteomics have greatly improved our capability to investigate the specificity of small molecules or fragments at the entire proteome scale.[57] Thus, more small molecules with exquisite specificity are within the reach for SMAP3-ID to investigate the subproteomes associated with a given protein, making it a broadly applicable method in native cellular environment. It is anticipated that SMAP3-ID will be complementary to other existing approaches for identifying protein−protein interactions. SMAP3-ID could be particularly useful to directly interrogate protein−protein interactions in patient-derived cells, where genetic engineering may not be feasible.

METHODS

Chemistry

All ^{1}H and ^{13}C NMR spectra were obtained in a Bruker Avance-Neo 400 MHz spectrometer in $CDCl_3$ or DMSO-d_6 using the chemical shifts of the residual $CHCl_3$ (δ 7.26) or DMSO (δ 2.50) as the reference. Chemical shifts (δ) are reported in parts per million (ppm), and the signal multiplicity is reported as brs (broad singlet), d (doublet), dd (doublet of doublets), td (triplet of doublets), m (multiplet), q (quartet), s (singlet), and t (triplet). Coupling constants (J values) are given in hertz. Purification by flash chromatography was performed using 230−400 mesh silica gel (EMD). Reaction progress was followed by thin-layer chromatography (TLC) on silica gel plates (EMD). Percent yields of final purified compounds is reported. Melting points were determined in capillary tubes using Mel-Temp and are uncorrected. The mass spectra of the small molecules were obtained from Advion PlateExpress by electrospray ionization in both positive and negative modes.

N-(1-Amino-7H-pyrrolo[3,2-*f*]quinazolin-3-yl)-4-(3-(trifluoromethyl)-3H-diazirin-3-yl)benzamide (2). To an Ar-flushed flask, compound **1** (45 mg, 0.11 mmol) prepared as previously described,[28] BOP (96 mg, 0.22 mmol), and DBU (33 mg, 0.22 mmol) were added. Freshly distilled THF (3 mL) was added to this mixture. The reaction mixture was stirred at room temperature in the dark for 4 h. Ammonia was condensed in a pressure tube at −78 °C (10 mL). The reaction mixture described above was then transferred to the pressure tube with liquid NH_3. The tube was sealed and stirred at room temperature in the dark overnight. The reaction mixture was cooled to −78 °C to open the pressure tube. The ammonia was allowed to evaporate as the mixture slowly cooled to room temperature. The remaining solvent was removed by rotary evaporation and the crude material was purified by flash chromatography eluting with EtOAc/DCM 4:1 with 1% Et_3N to afford **2** as a white solid (54%).

^{1}H NMR (400 MHz, DMSO-d_6) δ 11.83 (s, 1H), 10.64 (s, 1H), 8.08 (d, J = 8.4 Hz, 2H), 7.89 (d, J = 8.7 Hz, 1H), 7.60 (t, J = 2.4 Hz, 1H), 7.41 (d, J = 8.1 Hz, 2H), 7.34 (d, J = 8.8 Hz, 1H), 7.32−7.28 (m, 1H), 7.20 (brs, 2H); ESI-MS: Calcd for: $C_{19}H_{12}F_3N_7O$ $[M + H]^+$ 412.1 found 412.5.

N-(1-Amino-7-(2-azidoethyl)-7H-pyrrolo[3,2-*f*]quinazolin-3-yl)-4-(3-(trifluoromethyl)-3H-diazirin-3-yl)benzamide (LBL1-PCF). Compound **2** (9 mg, 0.022 mmol), NaI (2 mg, 0.011 mmol), and Cs_2CO_3 (13.8 mg, 0.044 mmol) were dissolved in anhydrous DMF (200 μL) under Ar in the dark. 1-Azidoethylbromide (0.066 mmol, 3 equiv) was dissolved in 600 μL of anhydrous DMF and added at a rate of 1 equiv per hour over 3 h at rt. Following the addition of the final equivalent of azidoethylbromide, the reaction mixture was stirred further for 1 hour at rt. Water (5 mL) was added, and the aqueous mixture was extracted with $CHCl_3$ (3 × 10 mL). The combined organic extracts were dried in Na_2SO_4 and concentrated to dryness. **LBL1-PCF** was obtained by silica gel flash chromatography (20:2:1 $CHCl_3$/THF/MeOH) as a pale-yellow solid (1.4 mg) in 14% yield.

^{1}H NMR (400 MHz, DMSO-d_6) δ 10.68 (s, 1 H), 8.08−8.16 (m, 3 H), 7.73 (d, J = 2.6 Hz, 1H), 7.47−7.44 (m, 3H), 7.41 (d, J = 2.8 Hz, 1H), 7.30 (brs, 2H), 4.60 (t, J = 5.8 Hz, 2H), 3.84 (t, J = 5.6 Hz, 2H); ^{13}C NMR (101 MHz, DMSO-d_6) δ 167.47, 162.10, 152.48, 136.66, 128.79, 126.26, 120.27. 120.12. 117.93, 102.56, 50.93, 45.08; ESI-MS: Calcd for: $C_{21}H_{15}F_3N_{10}O$ $[M + H]^+$ 481.1 found 481.5. HRESI-MS: Calcd for: $C_{21}H_{15}F_3N_{10}O$ $[M + H]^+$ 481.1461 found 481.1468.

Hex-5-ynal (5)

Compound **4** (400 mg, 4 mmol) was dissolved in dry DCM (20 mL), $PhI(OAc)_2$ (1.4 g, 4.4 mmol) and TEMPO (64 mg, 0.4 mmol) were added, and the reaction mixture was stirred for 2 h at rt. The reaction mixture was concentrated under vacuum, and the resulting residue was purified by flash chromatography (hexane/EtOAc 10:1) to afford **5** in a 44% yield as a yellow oil (178 mg).

https://doi.org/10.1021/jacsau.4c00988
JACS Au 2025, 5, 302−319

^{1}H NMR (400 MHz, $CDCl_3$) δ 9.81 (t, J = 1.3 Hz, 1 H), 2.61 (td, J = 7.2, 1.3 Hz, 2 H), 2.28 (td, J = 6.9, 2.8 Hz, 2 H), 1.98 (t, J = 2.6 Hz, 1 H), 1.86 (quintet, J = 7.1 Hz, 2 H).

4-(2-(Hex-5-yn-1-ylamino)ethyl)phenol (6)

Compound **5** (178 mg, 1.85 mmol) was dissolved in dry MeOH (5 mL) under Ar. Tyramine (254 mg, 1.85 mmol) was dissolved in dry MeOH (5 mL) and added to the reaction mixture. The reaction mixture was stirred overnight at rt. $NaBH_4$ (140 mg, 3.7 mmol) was added, and the reaction mixture was stirred for 1 h at rt. The solvent was removed by evaporation under reduced pressure, and the residue was subject to flash chromatography (15:1 DCM/MeOH) to afford **6** as a dark orange oily solid (145 mg) in a 38% yield.

^{1}H NMR (400 MHz, $CDCl_3$) δ 7.05 (d, J = 8.5 Hz, 2 H), 6.74 (d, J = 8.5 Hz, 2 H), 2.86 (t, J = 7.0 Hz, 2 H), 2.74 (t, J = 7.0 Hz, 2 H), 2.65 (t, J = 7.1 Hz, 2 H), 2.19 (td, J = 6.8, 2.4 Hz, 2 H), 1.93 (t, J = 2.7 Hz, 1 H), 1.76−1.56 (m, 2 H), 1.56−1.46 (m, 2 H); ESI-MS: Calcd for $C_{14}H_{20}NO$ $[M + H]^+$ 218.2; found 218.1.

tert-Butyl Hex-5-yn-1-yl(4-hydroxyphenethyl)carbamate (7)

Compound **6** (62 mg, 0.286 mmol) and Boc_2O (62 mg, 0.286 mmol) were dissolved in THF (1 mL). $NaHCO_3$ (24 mg, 0.286 mmol) was dissolved in H_2O (200 μL) and the solution was added. The reaction mixture was stirred for 2 h at rt until full protection was observed. The reaction mixture was diluted with H_2O (8 mL) and extracted with DCM (3 × 5 mL). The combined organic extracts were washed with $NaHCO_3$ (sat., aq. 1 × 5 mL) and brine (1 × 5 mL), dried over Na_2SO_4, and concentrated. Compound **7** was obtained as a clear colorless oil in a 99% yield (90 mg), and it was used directly for the next step without further purification.

^{1}H NMR (400 MHz, $CDCl_3$) δ 7.07 (d, J = 8.6 Hz, 2H), 6.78 (d, J = 8.6 Hz, 2H), 3.35 (t, J = 7.6 Hz, 2H), 3.16 (t, J = 7.3 Hz, 2H), 2.77 (t, J = 7.6 Hz, 2H), 2.22 (td, J = 7.0, 2.7 Hz, 2H), 1.97 (t, J = 2.6 Hz, 1H), 1.67−1.58 (m, 2H), 1.58−1.49 (m, 2H), 1.48 (s, 9H).

ESI-MS: Calcd for: $C_{19}H_{27}NO_3$ $[M\text{-}H]^-$ 316.2; found 316.1.

tert-Butyl hex-5-yn-1-yl(4-(2-(3-methyl-3*H*-diazirin-3-yl)ethoxy)-phenethyl)carbamate (9)

Compound **7** (62 mg, 0.195 mmol), compound **8**[32] (24 mg, 0.234 mmol), and PPh_3 (62 mg, 0.234 mmol) were placed in a sealed flask, which was then flushed with Ar. Anhydrous THF (2 mL) was added in the dark. The reaction mixture was cooled to 0 °C for 5 min, and then DIAD (48 mg, 0.234 mmol) was added dropwise. The reaction mixture was placed in a bath sonicator for 1 h and then stirred overnight at room temperature in the dark. The reaction mixture was concentrated and resuspended in hexanes. The resulting solid was removed by filtration. The crude mixture was purified by flash chromatography (6:1 EtOAc/Hexane) to afford **9** as a light-yellow oil (31 mg, 39% yield).

^{1}H NMR (400 MHz, $CDCl_3$) δ 7.09 (d, J = 8.8 Hz, 2H), 6.82 (d, J = 8.8 Hz, 2H), 3.85 (t, J = 6.3 Hz, 2H), 3.33 (t, J = 7.5 Hz, 2H), 3.16−3.12 (m, 2H), 2.76 (t, J = 7.7 Hz, 2H), 2.20 (td, J = 6.9 2.7 Hz, 2H), 1.94 (t, J = 2.6 Hz, 1H), 1.80 (t, J = 6.3 Hz, 2H), 1.61 (quintet, J = 7.6 Hz, 2H), 1.58−1.49 (m, 2H), 1.45 (s, 9H), 1.11 (s, 3H).

ESI-MS: Calcd for: $C_{23}H_{33}N_3O_3$ $[M + Na]^+$ 422.2; found 422.2.

N-(4-(2-(3-Methyl-3H-diazirin-3-yl)ethoxy)phenethyl)hex-5-yn-1-amine (10). Compound **9** (62 mg, 0.155 mmol) was dissolved in DCM (0.5 mL). TFA (225 mg, 9 mmol, 150 μL) was added, and the reaction mixture was stirred in the dark at room temperature for 2 h. $NaHCO_3$ (sat. aq. 10 mL) was added to the reaction mixture and stirred for 10 min. The aqueous mixture was extracted with DCM (3 × 5 mL), and the combined organic extracts were washed with brine. The organic solution was dried in Na_2SO_4 and concentrated. The crude mixture was purified by flash chromatography (15% MeOH in DCM) to afford clear colorless oil-to-solid **10** (45 mg, 98%).

^{1}H NMR (400 MHz, $CDCl_3$) δ 7.13 (d, J = 8.6 Hz, 2H), 6.82 (d, J = 8.6 Hz, 2H), 3.84 (t, J = 6.3 Hz, 2H), 2.98 (brs, 4H), 2.81 (t, J = 7.6 Hz, 2H), 2.20 (td, J = 7.0, 2.6 Hz, 2H), 1.92 (t, J = 2.7 Hz, 1H), 1.88−1.75 (m, 4H), 1.57 (q, J = 7.0 Hz, 2H), 1.11 (s, 3H).

ESI-MS: Calcd for: $C_{18}H_{25}N_3O$ $[M + H]^+$ 300.2; found 300.1.

DBCO−C6-N-(4-(2-(3-Methyl-3H-diazirin-3-yl)ethoxy)-phenethyl)hex-5-yn-1-amine (DDZ3). Compound **10** (11 mg, 0.038 mmol) and DBCO-C6-NHS ester (Click Chemistry Tools, 16 mg, 0.038 mmol) were dissolved in dry DMF (1 mL) under Ar in the dark. Et_3N (3.7 mg, 0.038 mmol) was added, and the reaction mixture was stirred at rt in the dark overnight. Water (10 mL) was added, and the mixture was extracted with DCM (3 × 5 mL) and EtOAc (3 × 5 mL). The organic extracts were combined, dried over Na_2SO_4, and concentrated. Purification by flash chromatography (7:1 DCM/EtOAc) afforded **DDZ3** as a thick yellow oil in 45% yield. Conformational isomers were observed in the NMR.

^{1}H NMR (400 MHz, DMSO-d_6) δ 7.65−7.53 (m, 2H), 7.43−7.52 (m, 3H), 7.40−7.30 (m, 2H), 7.28 (td, J = 6.9, 1.6 Hz, 1H), 7.08 (d, J = 8.6 Hz, 2H), 6.83 (d, J = 8.6 Hz, 2H), 5.04 (dd, J = 13.9, 4.9 Hz, 1H), 3.84 (t, J = 6.1 Hz, 2H), 3.60 (dd, J = 13.6, 4.6 Hz, 1H), 3.29−3.15 (m, 2H), 3.04 (t, J = 7.2 Hz, 1H), 2.72−2.77 (m, 1H), 2.69−2.57 (m, 2H), 2.19−2.08 (m, 3H), 2.04−1.94 (m, 1H), 1.84 (t, J = 7.3 Hz, 1H), 1.80−1.72 (m, 2H), 1.51−1.45 (m, 2H), 1.39−1.30 (m, 3H), 1.25−1.15 (m, 3H), 1.14−1.05 (m, 5H).

^{13}C NMR (101 MHz, DMSO-d_6) δ 171.68, 171.24, 171.11, 156.77, 151.86, 148.45, 132.41, 131.51, 130.81, 129.85, 129.58, 129.43, 128.85, 128.06, 127.98, 127.65, 126.75, 125.10, 122.48, 121.39, 114.42, 114.37, 108.20, 84.37, 84.13, 79.29, 78.97, 78.63, 71.38, 71.25, 62.71, 54.74, 48.66, 47.20, 46.83, 43.91, 33.93, 33.63, 33.42, 32.58, 31.63, 31.42, 27.63, 26.38, 25.35, 25.04, 24.60, 24.48, 24.17, 24.06, 19.70, 19.68, 17.48, 17.37; ESI-MS: Calcd for: $C_{39}H_{43}N_4O_3$ $[M + H]^+$ 615.3; found 615.5. HRESI-MS: Calcd for: $C_{39}H_{43}N_4O_3$ $[M + H]^+$ 615.3335; found 615.3342.

Cell Lines and Culture

MDA-MB-468 cells were purchased from the Developmental Therapeutics Program at the National Cancer Institute. MEFs with *LMNB1*$^{-/-}$*LMNB2*$^{-/-}$ (referred to as DKO) have been previously reported and were a generous gift of Professor Yixian Zheng (Carnegie Institution for Science).[13] We used DKO MEFs with LA knockdown as we described before.[13] The cells were tested for mycoplasma contamination regularly by PCR. Cells were cultured in high-glucose Dulbecco's modified Eagle's medium (DMEM, Life Technologies) supplemented with 10% FBS (Hyclone) and nonessential amino acids (Life Technologies) at 37 °C with 5% CO_2. All of the cells were authenticated using STR profiling and used within 50 passages.

Immunofluorescence

MDA-MB-468 cells were grown on poly-D-lysine (Sigma) coated coverslips. The cells were fixed with 4% formaldehyde and permeabilized with 0.3% Triton X-100 as previously described.[58] The cells were washed 2× with PBS and blocked with 3% BSA in PBS before incubating with primary antibodies overnight at 4 °C. The following primary antibodies were used: anti-LA/C (mouse, Sigma, Catalog No. SAB4200236, 1:8000), anti-EMD (rabbit, Cell Signaling Technology, catalog No. 30853, 1:400), anti-HNRNP-A2/B1 (rabbit, Thermo Scientific Invitrogen, catalog No. PA530061, 1:500), anti-HNRNP-M (rabbit, Cell Signaling Technology, catalog No. 88145, 1:500), anti-IDH3A (rabbit, Abcam, catalog No. ab228596, 1:100), anti-MDH2 (rabbit, Abcam, catalog No. ab96193, 1:100), anti-PDHA1 (rabbit, Abcam, catalog No. ab168379, 1:500), anti-SDHA (rabbit, Cell Signaling Technology, catalog No. 11998, 1:100), and anti-SRSF9 (rabbit, Thermo Scientific Invitrogen, catalog No. PA588610, 1:500). The cells were washed 3x with PBS at room temperature. The cells were then incubated with secondary antibodies for 1 h at 4 °C. AlexaFluor488 conjugated donkey antirabbit secondary antibody and AlexaFluor555 conjugated donkey antimouse antibody (Jackson Immunoresearch) were used at 1:1000 dilution in 3% BSA in PBS. The nuclei were counter-stained with DAPI (300 nM, Life Technologies), and the coverslips were mounted in ProLong Gold Anti-Fade reagent (Life Technologies). Images were acquired with Ziess LSM980.

https://doi.org/10.1021/jacsau.4c00988
JACS Au 2025, 5, 302−319

Western Blot

The lysates or immunoprecipitates were separated on 4−20% or Any kD TGX precast SDS-PAGE gels (Bio-Rad). Upon electrophoresis, the proteins were electrotransferred to nitrocellulose or PVDF membranes (Bio-Rad). The membranes were then blocked in 5% nonfat dry milk in TBST for 1 h at room temperature followed by incubation with primary antibodies at 4 °C overnight. The following primary antibodies were used: anti-LA/C (mouse, Sigma, Catalog No. SAB4200236, 1:2000), anti-Hsp90 (rabbit, Cell Signaling Technology, Catalog No. 4874, 1:1000), anti-LB1 (rabbit, Cell Signaling Technology, Catalog No. 12586, 1:1000), anti-GAPDH (mouse, Santa Cruz Biotechnology, Catalog No. sc-32233, 1:4000), anti-Histone 3 (H3) (mouse, Cell Signaling Technology, Catalog No. 14269, 1:1000), antiemerin (mouse, Sigma, Catalog No. MA5−31328, 1:1000), antiemerin (rabbit, Cell Signaling Technology, catalog No. 30853, 1:1000), anti-HNRNP-A2/B1 (rabbit, Thermo Scientific Invitrogen, catalog No. PA530061, 1:2500), anti-HNRNP-M (rabbit, Cell Signaling Technology, catalog No. 88145, 1:1000), anti-IDH3A (rabbit, Abcam, catalog No. ab228596, 1:5000), Anti-MDH2 (rabbit, Abcam, catalog No. ab96193, 1:2000), anti-PDHA1 (rabbit, Abcam, catalog No. ab168379, 1:2500), anti-SDHA (rabbit, Cell Signaling Technology, catalog No. 11998, 1:1000), anti-SRSF9 (rabbit, Thermo Scientific Invitrogen, catalog No. PA588610, 1:500−1000). The membranes were then washed 3x with TBST. Then, the membranes were incubated with HRP-conjugated secondary antibodies (Jackson ImmunoResearch Laboratories, 1:4000) in 5% nonfat dry milk in TBST for 1 h at room temperature. For streptavidin blot, the blocked membranes were incubated with HRP-streptavidin (Jackson ImmunoResearch Laboratories, 1:100,000 in TBST) for 1 h at room temperature. The membranes were then washed 3x with TBST and imaged using Clarity Western ECL Substrate (Bio-Rad) in ChemiDoc^{MP} (Bio-Rad).

LBL1-PCF Photo-Cross-Linking and Click Chemistry

MDA-MB-468 cells grown to 80% confluence were washed once with PBS. Then, the cells were incubated with indicated concentrations of **LBL1-PCF** in PBS for 30 min at 37 °C. The cells were then cooled to 4 °C followed by irradiation at 365 nm light (UV Cross-linker FB-UVXL-1000, Fisher Scientific) for 3 min at 4 °C. The cells were then collected and washed twice with cold PBS. Then, the cells were lysed in 1% SDS in PBS with gentle sonication. The lysates were cleared by centrifuging at 14,000x rpm for 10 min. The protein concentration of the lysates was determined by a BCA Protein Assay Kit (Pierce). Equal amounts of proteins were then subjected to click reaction with the biotin-alkyne or biotin-dde-alkyne (10 μM), TCEP (1 mM), TBTA (100 μM), $CuSO_4$ (1 mM) for 1 h at room temperature in the dark. The SDS concentration in the click reaction mixture was controlled to be <0.5%. SDS-PAGE sample buffer was added and the lysates were loaded onto precast SDS-PAGE gels for electrophoresis followed by Western blot analyses.

Streptavidin Enrichment

The click reaction mixture derived from biotin-alkyne or biotin-N_3 was mixed with an equal volume of methanol and 0.25x volume of chloroform for a final volume ratio of reaction mixture:MeOH:$CHCl_3$ (4:4:1). The mixture was shaken vigorously for 30 s and then centrifuged at 8,000x g for 10 min at room temperature. The supernatant was discarded and the resulting protein solids were washed three times with 1:1 MeOH−$CHCl_3$ and then immediately resuspended in MeOH. To ensure the full suspension of the protein solids, the solids were mechanically broken up followed by sonication. $CHCl_3$ was added to the suspension for a final MeOH−$CHCl_3$ ratio of 4:1. The solution was shaken vigorously for 30 s. The mixture was centrifuged for 10 min at 14,000× rpm. The resulting protein solid was redissolved in 1% SDS in PBS. The lysate protein concentrations were redetermined with a BCA Protein Assay Kit (Pierce). Equal amounts of proteins were taken from each reaction and diluted with PBS to a final 0.1% SDS concentration, which was then tumbled with PBS-washed streptavidin agarose beads overnight at room temperature. The beads were pelleted by centrifugation at 3,000x rpm for 2 min. The supernatant was removed, and the beads were then washed three times with 1% SDS in PBS followed by six times with PBS. The bound proteins were eluted with 1% SDS/PBS containing 1 mM free biotin at 95 °C for 5 min. The eluates were analyzed by Western blot. For proteomics analysis, the beads were further washed with 2 × 100 μL of 100 mM NH_4HCO_3 after biotin elution. The elution and washes were combined for proteomics analysis, as described below.

LC-MS/MS Analysis

Affinity-purified proteins from above were dried by vacuum centrifugation and redissolved in 150 μL of 5% SDS in 50 mM triethylammonium bicarbonate (TEAB). Samples were reduced with dithiothreitol and alkylated with idoacetamide followed by trypsin digestion on S-Trap micro (Protifi, Inc.) according to the manufacturer's suggested protocol. After digestion overnight at 37 °C, the peptides were eluted with 40 μL of 50 mM TEAB, followed by 0.2% formic acid in ddI H_2O and 50% acetonitrile in ddI H_2O containing 0.2% formic acid. The elutions were pooled, dried in a SpeedVac, redissolved in 20 μL of 5% formic acid, and subjected to LC/MS/MS analysis.

Each peptide elution from above was then chromatographically separated using a Dionex RSLC UHPLC system and delivered to a Q-Exactive HF mass spectrometer (Thermo Scientific) using electrospray ionization with a Nano Flex Ion Spray Source fitted with a 20 μm stainless steel nanobore emitter spray tip and 1.0 kV source voltage. Xcalibur version 4.0 was used to control the system. Samples were applied at 10 μL/min to a Symmetry C18 trap cartridge (Waters) for 5 min and then switched onto a 75 μm × 250 mm NanoAcquity BEH 130 C18 column with 1.7 μm particles (Waters) using mobile phases water (A) and acetonitrile (B) containing 0.1% formic acid, 7.5−30% acetonitrile gradient over 60 min, and 300 nL/min flow rate. Survey mass spectra were acquired over m/z 375−1400 at 120,000 resolution (m/z 200) and data-dependent acquisition selected the top 10 most abundant precursor ions for tandem mass spectrometry by HCD fragmentation using an isolation width of 1.2 m/z, normalized collision energy of 30, and a resolution of 30,000. Dynamic exclusion was set to auto, charge state for MS/MS + 2 to +7, maximum ion time 100 ms, minimum AGC target of 3×10^6 in MS1 mode and 5×10^3 in MS2 mode.

Comet (v. 2016.01, rev. 3)[59] was used to search 132,271 MS2 spectra against a UniProt human Swiss-Prot protein FASTA collection (v2022.10 with 20,366 sequences). The FASTA file was augmented with 179 common contaminant sequences and concatenated sequence-reversed entries of all proteins (to estimate error thresholds). The database processing used Python scripts available at https://github.com/pwilmart/fasta_utilities.git and Comet results processing used the PAW pipeline[60] from https://github.com/pwilmart/PAW_pipeline.git. Comet searches for all samples were performed with trypsin enzyme specificity (maximum of two missed cleavages) with the monoisotopic parent ion mass tolerance set to 1.25 Da and the monoisotopic fragment ion mass tolerance set at 0.02 Da. A static modification of +57.02146 Da was added to all cysteine residues and a variable modification of +15.9949 Da on methionine residues. Comet scores were combined into linear discriminant function scores,[60,61] and discriminant score histograms created separately for each peptide charge state (2+, 3+, and 4+). Separate histograms were created for peptide-spectrum-matches (PSMs) to forward sequences and for matches to reversed sequences for all peptides of seven amino acids or longer. The score histograms of reversed matches were used to estimate PSM false discovery rates (FDR) and set score thresholds for each PSM class at 2%. There were 26,000 PSMs passing thresholds and mapped to proteins using basic and extended parsimony principles. There were 1818 proteins (including contaminants and decoy proteins) inferred using a two distinct peptide sequences per protein requirement with a false discovery rate (FDR) of <1.7%.

https://doi.org/10.1021/jacsau.4c00988
JACS Au 2025, 5, 302−319

SPAAC between LBL1-PCF and DBCO-Containing Compounds in MDA-MB-468 Cells

MDA-MB-468 cells were treated with **LBL1-PCF** for photo-cross-linking as described above. After UV irradiation, the cells were washed twice with full media (5−10 min at 37 °C per wash). The wash media was replaced and the cells were incubated with **DDZ3**, **CP2039**, or **TAMRA-DBCO** (Click Chemistry Tools) at indicated concentrations in full media for 2 h at 37 °C. When a second UV irradiation was applied, the **LBL1-PCF**- and **DDZ3**-treated cells were further washed 3 times with PBS. Then, the cells in PBS were further irradiated at 365 nm for 5 min. The cells were washed with PBS followed by fixing/permeabilization for confocal microscopy, or the cells were collected and lysed for click reaction with biotin-azide or biotin-alkyne as described above.

Coimmunoprecipitation

Untreated MDA-MB-468 cells at 80% confluence were collected mechanically and then washed twice with ice-cold PBS. The cell pellets were lysed in lysis buffer B (50 mM Tris, 5 mM EDTA, 150 mM NaCl, 1 mM DTT, and 0.5% Nonidet P-40, pH 8.0) supplemented with 1 mM PMSF and protease inhibitor cocktail (4 mg/mL, Pierce). The lysates were centrifuged at 14,000× rpm for 20 min at 4 °C. The protein concentration was determined using BCA Protein Assay Kit (Pierce). The lysates were subject to an initial preclearance step by tumbling with mouse IgG (Jackson ImmunoResearch) and Pierce protein A/G ultralink agarose beads (Thermos Scientific) at 4 °C for 1 h. The precleared lysates were then tumbled overnight with anti-LA or IgG at 4 °C. Protein A/G beads were added and tumbled for 1 h at 4 °C. The agarose beads were separated from the unbound flow through by centrifugation (3000× rpm, 2 min, 4 °C). The beads were then washed three times with lysis buffer B at 4 °C. The bound proteins were eluted from the beads with 1× SDS-PAGE loading buffer at 95 °C for 5 min. The eluted proteins were analyzed by SDS-PAGE followed by Western blot.

Live Cell Imaging of Mitochondria

MDA-MB-468 cells were plated on poly-D-Lysine (Sigma) coated 24-well glass bottom plates in FluoroBrite DMEM (Thermo Fisher) supplemented with nonessential amino acids (Thermo Fisher) and 10% FBS (2×10^5 cells/well) for 24 h at 37 °C. The cells were treated with DMSO or 5 μM **LBL1** for 18 h at 37 °C. Then, mitochondrial dye MitoView640 Fix (Biotium) was added at the final concentration of 200 nM for 30 min at 37 °C. The live cells were then imaged on Spinning Disk-Nikon/Yokogawa CSU-W1. About 30 images were acquired per condition.

Mitochondrial Morphology Analysis

The 3D stacks of live mitochondrial images acquired from above were deconvolved by using Imaris 10.1. Further analysis of these 3D images was done using the Mitochondria Analyzer Plug in ImageJ. Each image was converted to a binary image using batch conversion with optimized thresholding with a C value of 5 and a block size of 1.45. The thresholded images were then subject to mitochondrial analysis on per mitochondrial and per cell bases. For the per cell basis, each region of interest (ROI) was analyzed as a single cell.

Lactate Assay

MDA-MB-468 cells were plated on a six-well plate (9×10^5 cells/well) and allowed to attach overnight at 37 °C. The cells were treated with DMSO or **LBL1** (5 μM) and incubated at 37 °C for 18 h. The cells were washed once with FBS-free DMEM. Then, FBS-free DMEM containing **LBL1** (0 or 5 μM) and oligomycin (0 or 5 μM) were added and incubated for two hours at 37 °C. An aliquot of media was collected (40 μL per well) for lactate measurement. The cells were collected mechanically and were fully resuspended. An aliquot of the cell suspension was incubated with 0.4% Trypan blue solution for 2 min. The number of live cells was counted by using a hemocytometer. The extracellular lactate concentration was determined using Lactate-Glo assay (Promega) according to the manufacturer's protocol. Briefly, the lactate concentrations were determined after dilution in FBS-free DMEM (10x dilution for samples without oligomycin and 100x dilution for samples treated with oligomycin). The diluted sample was then mixed with the freshly prepared Lactate-Glo reagent in equal portions (10 μL from the sample and 10 μL of reagent) in a white-bottom 384-well plate. A series of lactate standards were prepared in FBS-free DMEM and mixed with Lactate-Glo reagent solution in the same 384-well plate. The plate was shaken for 2 min at rt and then incubated at rt for 1 h. The luminescence was measured using a Tecan plate reader. The lactate concentrations for each sample were determined by using the standard curve. The lactate concentration was normalized to the cell count from the corresponding well.

ATP Assay

MDA-MB-468 cells were plated in a white-bottom 96-well plate at 3×10^4 cells per well. The cells were treated with DMSO or **LBL1** (5 μM) for 18 h at 37 °C, when the cells were further treated with oligomycin (0 or 5 μM) along with or without 2-DG (22.5 mM) for 2 h at 37 °C. The cellular ATP level was then measured using CellTiter-Glo 2.0 assay kit (Promega) according to the manufacturer's protocol. Briefly, the assay reagent was added (80 μL reagent added to the remaining 80 μL media), and the plate was shaken for 2 min on an orbital shaker at room temperature. The plate was further incubated at room temperature for 10 min. The luminescence was then measured using a Tecan plate reader. To normalize the cellular ATP levels, a separate set of MDA-MB-468 cells in a 96-well plate were prepared and treated identically to those for the ATP assay. At the end of treatment, the media were completely removed, and the cells were lysed in lysis buffer B (50 μL). The protein concentrations were determined by the BCA protein assay (Thermo Scientific). The average protein concentration from each condition was used to normalize the luminescence signal obtained in the ATP assay. The relative bioenergetic organization was calculated as previously described.[47] The contribution from mitochondrial respiration was calculated by subtracting the normalized ATP in the presence of oligomycin from the total normalized cellular ATP. The remaining ATP was treated as glycolytic ATP.

■ ASSOCIATED CONTENT

Supporting Information

The Supporting Information is available free of charge at https://pubs.acs.org/doi/10.1021/jacsau.4c00988.

Proteins identified by **LBL1-PCF** (Table S1) (XLSX)

Proteins identified by **LBL1-PCF** along with **DDZ3** (Table S2) (XLSX)

Full GO terms (Table S3) (XLSX)

Additional analysis by Western blotting, confocal microscopy, chemoproteomics, and mitochondrial morphology (Figures S1−S10) (PDF)

Comparison of identified lamina-omes by different methods (Table S4) (XLSX)

■ AUTHOR INFORMATION

Corresponding Authors

Xiangshu Xiao − *Program in Chemical Biology, Department of Chemical Physiology and Biochemistry and Knight Cancer Institute, Oregon Health & Science University, Portland, Oregon 97239, United States;* orcid.org/0000-0001-9520-1371; Email: xiaoxi@ohsu.edu

Bingbing X. Li − *Program in Chemical Biology, Department of Chemical Physiology and Biochemistry and Knight Cancer Institute, Oregon Health & Science University, Portland, Oregon 97239, United States;* orcid.org/0000-0001-8259-9448; Email: lib@ohsu.edu

https://doi.org/10.1021/jacsau.4c00988
JACS Au 2025, 5, 302−319

Authors

Julia Warren − *Program in Chemical Biology, Department of Chemical Physiology and Biochemistry, Oregon Health & Science University, Portland, Oregon 97239, United States*

Jian Wang − *Program in Chemical Biology, Department of Chemical Physiology and Biochemistry, Oregon Health & Science University, Portland, Oregon 97239, United States;* orcid.org/0000-0003-0806-9590

Francis Dhoro − *Program in Chemical Biology, Department of Chemical Physiology and Biochemistry, Oregon Health & Science University, Portland, Oregon 97239, United States*

Bo Chao − *Program in Chemical Biology, Department of Chemical Physiology and Biochemistry, Oregon Health & Science University, Portland, Oregon 97239, United States;* orcid.org/0000-0002-4186-8354

Ashok Reddy − *Proteomics Shared Resources, Oregon Health & Science University, Portland, Oregon 97239, United States*

Stefanie Kaech Petrie − *Knight Cancer Institute and Department of Neurology, Oregon Health & Science University, Portland, Oregon 97239, United States*

Larry L. David − *Program in Chemical Biology, Department of Chemical Physiology and Biochemistry and Knight Cancer Institute, Oregon Health & Science University, Portland, Oregon 97239, United States*

Complete contact information is available at: https://pubs.acs.org/10.1021/jacsau.4c00988

Notes

The authors declare no competing financial interest.

■ ACKNOWLEDGMENTS

This work was made possible by financial support provided by R21EB028425 (B.X.L.), R01CA245964 (B.X.L.), R01CA211866 (X.X.), R01GM122820 (X.X.), and R01CA278058 (B.X.L. and X.X.). We thank OHSU Gene Profiling Shared Resource for authenticating the cell lines through STR profiling and OHSU Advanced Light Microscopy Shared Resource for providing technical support. The OHSU Advanced Light Microscopy Shared Resource and Gene Profiling Shared Resource were partially supported by P30CA069533. Mass spectrometric analysis was performed by the OHSU Proteomics Shared Resource with partial support from NIH core grants P30EY010572, P30CA069533, and OHSU Emerging Technology Fund.

■ REFERENCES

(1) Huttlin, E. L.; Bruckner, R. J.; Paulo, J. A.; Cannon, J. R.; Ting, L.; Baltier, K.; Colby, G.; Gebreab, F.; Gygi, M. P.; Parzen, H.; Szpyt, J.; Tam, S.; Zarraga, G.; Pontano-Vaites, L.; Swarup, S.; White, A. E.; Schweppe, D. K.; Rad, R.; Erickson, B. K.; Obar, R. A.; Guruharsha, K. G.; Li, K.; Artavanis-Tsakonas, S.; Gygi, S. P.; Harper, J. W. Architecture of the human interactome defines protein communities and disease networks. *Nature* **2017**, *545* (7655), 505−509.

(2) Vidal, M.; Cusick, M. E.; Barabási, A. L. Interactome networks and human disease. *Cell* **2011**, *144* (6), 986−998.

(3) Rogawski, R.; Sharon, M. Characterizing Endogenous Protein Complexes with Biological Mass Spectrometry. *Chem. Rev.* **2022**, *122* (8), 7386−7414.

(4) Roberts, A. W.; Davids, M. S.; Pagel, J. M.; Kahl, B. S.; Puvvada, S. D.; Gerecitano, J. F.; Kipps, T. J.; Anderson, M. A.; Brown, J. R.; Gressick, L.; Wong, S.; Dunbar, M.; Zhu, M.; Desai, M. B.; Cerri, E.; Heitner Enschede, S.; Humerickhouse, R. A.; Wierda, W. G.; Seymour, J. F. Targeting BCL2 with Venetoclax in Relapsed Chronic Lymphocytic Leukemia. *N. Engl. J. Med.* **2016**, *374* (4), 311−322.

(5) Reck, M.; Rodríguez-Abreu, D.; Robinson, A. G.; Hui, R.; Csőszi, T.; Fülöp, A.; Gottfried, M.; Peled, N.; Tafreshi, A.; Cuffe, S.; O'Brien, M.; Rao, S.; Hotta, K.; Leiby, M. A.; Lubiniecki, G. M.; Shentu, Y.; Rangwala, R.; Brahmer, J. R. Pembrolizumab versus Chemotherapy for PD-L1-Positive Non-Small-Cell Lung Cancer. *N. Engl. J. Med.* **2016**, *375* (19), 1823−1833.

(6) Burke, B.; Stewart, C. L. The nuclear lamins: flexibility in function. *Nat. Rev. Mol. Cell Biol.* **2013**, *14* (1), 13−24.

(7) Gerace, L.; Blum, A.; Blobel, G. Immunocytochemical localization of the major polypeptides of the nuclear pore complex-lamina fraction. Interphase and mitotic distribution. *J. Cell Biol.* **1978**, *79* (2 Pt 1), 546−566.

(8) Aebi, U.; Cohn, J.; Buhle, L.; Gerace, L. The nuclear lamina is a meshwork of intermediate-type filaments. *Nature* **1986**, *323* (6088), 560−564.

(9) Shumaker, D. K.; Solimando, L.; Sengupta, K.; Shimi, T.; Adam, S. A.; Grunwald, A.; Strelkov, S. V.; Aebi, U.; Cardoso, M. C.; Goldman, R. D. The highly conserved nuclear lamin Ig-fold binds to PCNA: its role in DNA replication. *J. Cell Biol.* **2008**, *181* (2), 269−280.

(10) Gerace, L.; Tapia, O. Messages from the voices within: regulation of signaling by proteins of the nuclear lamina. *Curr. Opin. Cell Biol.* **2018**, *52*, 14−21.

(11) Varela, I.; Cadinanos, J.; Pendas, A. M.; Gutierrez-Fernandez, A.; Folgueras, A. R.; Sanchez, L. M.; Zhou, Z.; Rodriguez, F. J.; Stewart, C. L.; Vega, J. A.; Tryggvason, K.; Freije, J. M.; Lopez-Otin, C. Accelerated ageing in mice deficient in Zmpste24 protease is linked to p53 signalling activation. *Nature* **2005**, *437* (7058), 564−568.

(12) Lammerding, J.; Schulze, P. C.; Takahashi, T.; Kozlov, S.; Sullivan, T.; Kamm, R. D.; Stewart, C. L.; Lee, R. T. Lamin A/C deficiency causes defective nuclear mechanics and mechanotransduction. *J. Clin. Invest.* **2004**, *113* (3), 370−378.

(13) Li, B. X.; Chen, J.; Chao, B.; Zheng, Y.; Xiao, X. A Lamin-Binding Ligand Inhibits Homologous Recombination Repair of DNA Double-Strand Breaks. *ACS Cent. Sci.* **2018**, *4* (9), 1201−1210.

(14) Petillo, R.; D'Ambrosio, P.; Torella, A.; Taglia, A.; Picillo, E.; Testori, A.; Ergoli, M.; Nigro, G.; Piluso, G.; Nigro, V.; Politano, L. Novel mutations in LMNA A/C gene and associated phenotypes. *Acta Myol.* **2015**, *34* (2−3), 116−119.

(15) Broers, J. L. V.; Ramaekers, F. C.; Bonne, G.; Yaou, R. B.; Hutchison, C. J. Nuclear lamins: laminopathies and their role in premature ageing. *Physiol. Rev.* **2006**, *86* (3), 967−1008.

(16) Butin-Israeli, V.; Adam, S. A.; Goldman, A. E.; Goldman, R. D. Nuclear lamin functions and disease. *Trends Genet.* **2012**, *28* (9), 464−471.

(17) Wong, X.; Melendez-Perez, A. J.; Reddy, K. L. The Nuclear Lamina. *Cold Spring Harb. Perspect. Biol.* **2022**, *14* (2), No. a040113, DOI: 10.1101/cshperspect.a040113.

(18) Moir, R. D.; Donaldson, A. D.; Stewart, M. Expression in *Escherichia coli* of human lamins A and C: influence of head and tail domains on assembly properties and paracrystal formation. *J. Cell Sci.* **1991**, *99*, 363−372.

(19) Aaronson, R. P.; Blobel, G. Isolation of nuclear pore complexes in association with a lamina. *Proc. Natl. Acad. Sci. U.S.A.* **1975**, *72* (3), 1007−1011.

(20) Roux, K. J.; Kim, D. I.; Raida, M.; Burke, B. A promiscuous biotin ligase fusion protein identifies proximal and interacting proteins in mammalian cells. *J. Cell Biol.* **2012**, *196* (6), 801−810.

(21) Kubben, N.; Voncken, J. W.; Misteli, T. Mapping of protein- and chromatin-interactions at the nuclear lamina. *Nucleus* **2010**, *1* (6), 460−471.

(22) Fu, Y.; Lv, P.; Yan, G.; Fan, H.; Cheng, L.; Zhang, F.; Dang, Y.; Wu, H.; Wen, B. MacroH2A1 associates with nuclear lamina and maintains chromatin architecture in mouse liver cells. *Sci. Rep.* **2015**, *5*, No. 17186.

(23) Dittmer, T. A.; Sahni, N.; Kubben, N.; Hill, D. E.; Vidal, M.; Burgess, R. C.; Roukos, V.; Misteli, T. Systematic identification of

pathological lamin A interactors. *Mol. Biol. Cell* **2014**, *25* (9), 1493−1510.
(24) Depreux, F. F.; Puckelwartz, M. J.; Augustynowicz, A.; Wolfgeher, D.; Labno, C. M.; Pierre-Louis, D.; Cicka, D.; Kron, S. J.; Holaska, J.; McNally, E. M. Disruption of the lamin A and matrin-3 interaction by myopathic LMNA mutations. *Hum. Mol. Genet.* **2015**, *24* (15), 4284−4295.
(25) Engelke, R.; Riede, J.; Hegermann, J.; Wuerch, A.; Eimer, S.; Dengjel, J.; Mittler, G. The quantitative nuclear matrix proteome as a biochemical snapshot of nuclear organization. *J. Proteome Res.* **2014**, *13* (9), 3940−3956.
(26) Bar, D. Z.; Atkatsh, K.; Tavarez, U.; Erdos, M. R.; Gruenbaum, Y.; Collins, F. S. Biotinylation by antibody recognition-a method for proximity labeling. *Nat. Methods* **2018**, *15* (2), 127−133.
(27) Tran, J. R.; Paulson, D. I.; Moresco, J. J.; Adam, S. A.; Yates, J. R.; Goldman, R. D.; Zheng, Y. An APEX2 proximity ligation method for mapping interactions with the nuclear lamina. *J. Cell Biol.* **2021**, *220* (1), No. e202002129, DOI: 10.1083/jcb.202002129.
(28) Li, B. X.; Chen, J.; Chao, B.; David, L. L.; Xiao, X. Anticancer pyrroloquinazoline LBL1 targets nuclear lamins. *ACS Chem. Biol.* **2018**, *13*, 1380−1387.
(29) Agard, N. J.; Prescher, J. A.; Bertozzi, C. R. A strain-promoted [3 + 2] azide-alkyne cycloaddition for covalent modification of biomolecules in living systems. *J. Am. Chem. Soc.* **2004**, *126* (46), 15046−15047.
(30) Xiao, X.; Li, B. X. Identification of lamins as the molecular targets of LBL1 using a clickable photoaffinity probe. *Methods Enzymol.* **2020**, *633*, 185−201.
(31) Guo, Y.; Kim, Y.; Shimi, T.; Goldman, R. D.; Zheng, Y. Concentration-dependent lamin assembly and its roles in the localization of other nuclear proteins. *Mol. Biol. Cell* **2014**, *25* (8), 1287−1297.
(32) Martín-Acosta, P.; Meng, Q.; Klimek, J.; Reddy, A. P.; David, L.; Petrie, S. K.; Li, B. X.; Xiao, X. A clickable photoaffinity probe of betulinic acid identifies tropomyosin as a target. *Acta Pharm. Sin. B* **2022**, *12* (5), 2406−2416.
(33) van Geel, R.; Pruijn, G. J.; van Delft, F. L.; Boelens, W. C. Preventing thiol-yne addition improves the specificity of strain-promoted azide-alkyne cycloaddition. *Bioconjugate Chem.* **2012**, *23* (3), 392−398.
(34) Kolberg, L.; Raudvere, U.; Kuzmin, I.; Adler, P.; Vilo, J.; Peterson, H. g:Profiler-interoperable web service for functional enrichment analysis and gene identifier mapping (2023 update). *Nucleic Acids Res.* **2023**, *51* (W1), W207−W212.
(35) Lee, K. K.; Haraguchi, T.; Lee, R. S.; Koujin, T.; Hiraoka, Y.; Wilson, K. L. Distinct functional domains in emerin bind lamin A and DNA-bridging protein BAF. *J. Cell Sci.* **2001**, *114* (Pt 24), 4567−4573.
(36) Nmezi, B.; Xu, J.; Fu, R.; Armiger, T. J.; Rodriguez-Bey, G.; Powell, J. S.; Ma, H.; Sullivan, M.; Tu, Y.; Chen, N. Y.; Young, S. G.; Stolz, D. B.; Dahl, K. N.; Liu, Y.; Padiath, Q. S. Concentric organization of A- and B-type lamins predicts their distinct roles in the spatial organization and stability of the nuclear lamina. *Proc. Natl. Acad. Sci. U.S.A.* **2019**, *116* (10), 4307−4315.
(37) Li, W.; Long, Q.; Wu, H.; Zhou, Y.; Duan, L.; Yuan, H.; Ding, Y.; Huang, Y.; Wu, Y.; Huang, J.; Liu, D.; Chen, B.; Zhang, J.; Qi, J.; Du, S.; Li, L.; Liu, Y.; Ruan, Z.; Liu, Z.; Liu, Z.; Zhao, Y.; Lu, J.; Wang, J.; Chan, W. Y.; Liu, X. Nuclear localization of mitochondrial TCA cycle enzymes modulates pluripotency via histone acetylation. *Nat. Commun.* **2022**, *13* (1), No. 7414.
(38) Maynard, S.; Hall, A.; Galanos, P.; Rizza, S.; Yamamoto, T.; Gram, H. H.; Munk, S. H. N.; Shoaib, M.; Sørensen, C. S.; Bohr, V. A.; Lerdrup, M.; Maya-Mendoza, A.; Bartek, J. Lamin A/C impairments cause mitochondrial dysfunction by attenuating PGC1α and the NAMPT-NAD+ pathway. *Nucleic Acids Res.* **2022**, *50* (17), 9948−9965.
(39) Lopez-Mejia, I. C.; de Toledo, M.; Chavey, C.; Lapasset, L.; Cavelier, P.; Lopez-Herrera, C.; Chebli, K.; Fort, P.; Beranger, G.; Fajas, L.; Amri, E. Z.; Casas, F.; Tazi, J. Antagonistic functions of LMNA isoforms in energy expenditure and lifespan. *EMBO Rep.* **2014**, *15* (5), 529−539.
(40) Rivera-Torres, J.; Acín-Perez, R.; Cabezas-Sánchez, P.; Osorio, F. G.; Gonzalez-Gómez, C.; Megias, D.; Cámara, C.; López-Otín, C.; Enríquez, J. A.; Luque-García, J. L.; Andrés, V. Identification of mitochondrial dysfunction in Hutchinson-Gilford progeria syndrome through use of stable isotope labeling with amino acids in cell culture. *J. Proteomics* **2013**, *91*, 466−477.
(41) Chaudhry, A.; Shi, R.; Luciani, D. S. A pipeline for multidimensional confocal analysis of mitochondrial morphology, function, and dynamics in pancreatic β-cells. *Am. J. Physiol. Endocrinol. Metab.* **2020**, *318* (2), E87−E101.
(42) Lardy, H. A.; Johnson, D.; Mc, M. W. Antibiotics as tools for metabolic studies. I. A survey of toxic antibiotics in respiratory, phosphorylative and glycolytic systems. *Arch. Biochem. Biophys.* **1958**, *78* (2), 587−597.
(43) Symersky, J.; Osowski, D.; Walters, D. E.; Mueller, D. M. Oligomycin frames a common drug-binding site in the ATP synthase. *Proc. Natl. Acad. Sci. U.S.A.* **2012**, *109* (35), 13961−13965.
(44) Lim, S. O.; Li, C. W.; Xia, W.; Lee, H. H.; Chang, S. S.; Shen, J.; Hsu, J. L.; Raftery, D.; Djukovic, D.; Gu, H.; Chang, W. C.; Wang, H. L.; Chen, M. L.; Huo, L.; Chen, C. H.; Wu, Y.; Sahin, A.; Hanash, S. M.; Hortobagyi, G. N.; Hung, M. C. EGFR Signaling Enhances Aerobic Glycolysis in Triple-Negative Breast Cancer Cells to Promote Tumor Growth and Immune Escape. *Cancer Res.* **2016**, *76* (5), 1284−1296.
(45) Urra, F. A.; Muñoz, F.; Córdova-Delgado, M.; Ramírez, M. P.; Peña-Ahumada, B.; Rios, M.; Cruz, P.; Ahumada-Castro, U.; Bustos, G.; Silva-Pavez, E.; Pulgar, R.; Morales, D.; Varela, D.; Millas-Vargas, J. P.; Retamal, E.; Ramírez-Rodríguez, O.; Pessoa-Mahana, H.; Pavani, M.; Ferreira, J.; Cárdenas, C.; Araya-Maturana, R. FR58P1a; a new uncoupler of OXPHOS that inhibits migration in triple-negative breast cancer cells via Sirt1/AMPK/β1-integrin pathway. *Sci. Rep.* **2018**, *8* (1), No. 13190.
(46) Dwarakanath, B.; Jain, V. Targeting glucose metabolism with 2-deoxy-D-glucose for improving cancer therapy. *Future Oncol.* **2009**, *5* (5), 581−585.
(47) Hao, W.; Chang, C. P.; Tsao, C. C.; Xu, J. Oligomycin-induced bioenergetic adaptation in cancer cells with heterogeneous bioenergetic organization. *J. Biol. Chem.* **2010**, *285* (17), 12647−12654.
(48) Zervopoulos, S. D.; Boukouris, A. E.; Saleme, B.; Haromy, A.; Tejay, S.; Sutendra, G.; Michelakis, E. D. MFN2-driven mitochondria-to-nucleus tethering allows a non-canonical nuclear entry pathway of the mitochondrial pyruvate dehydrogenase complex. *Mol. Cell* **2022**, *82* (5), 1066−1077.e7.
(49) Nagaraj, R.; Sharpley, M. S.; Chi, F.; Braas, D.; Zhou, Y.; Kim, R.; Clark, A. T.; Banerjee, U. Nuclear Localization of Mitochondrial TCA Cycle Enzymes as a Critical Step in Mammalian Zygotic Genome Activation. *Cell* **2017**, *168* (1−2), 210−223.e11.
(50) Liu, X.; Si, W.; He, L.; Yang, J.; Peng, Y.; Ren, J.; Liu, X.; Jin, T.; Yu, H.; Zhang, Z.; Cheng, X.; Zhang, W.; Xia, L.; Huang, Y.; Wang, Y.; Liu, S.; Shan, L.; Zhang, Y.; Yang, X.; Li, H.; Liang, J.; Sun, L.; Shang, Y. The existence of a nonclassical TCA cycle in the nucleus that wires the metabolic-epigenetic circuitry. *Signal Transduction Targeted Ther.* **2021**, *6* (1), No. 375.
(51) Kafkia, E.; Andres-Pons, A.; Ganter, K.; Seiler, M.; Smith, T. S.; Andrejeva, A.; Jouhten, P.; Pereira, F.; Franco, C.; Kuroshchenkova, A.; Leone, S.; Sawarkar, R.; Boston, R.; Thaventhiran, J.; Zaugg, J. B.; Lilley, K. S.; Lancrin, C.; Beck, M.; Patil, K. R. Operation of a TCA cycle subnetwork in the mammalian nucleus. *Sci.e Adv.* **2022**, *8* (35), No. eabq5206.
(52) Arnold, R.; Vehns, E.; Randl, H.; Djabali, K. Baricitinib, a JAK-STAT Inhibitor, Reduces the Cellular Toxicity of the Farnesyltransferase Inhibitor Lonafarnib in Progeria Cells. *Int. J. Mol. Sci.* **2021**, *22* (14), No. 7474, DOI: 10.3390/ijms22147474.
(53) Choudhury, D.; Rong, N.; Ikhapoh, I.; Rajabian, N.; Tseropoulos, G.; Wu, Y.; Mehrotra, P.; Thiyagarajan, R.; Shahini, A.; Seldeen, K. L.; Troen, B. R.; Lei, P.; Andreadis, S. T. Inhibition of

glutaminolysis restores mitochondrial function in senescent stem cells. *Cell Rep.* **2022**, *41* (9), No. 111744.
(54) Pavlova, N. N.; Zhu, J.; Thompson, C. B. The hallmarks of cancer metabolism: Still emerging. *Cell Metab.* **2022**, *34* (3), 355−377.
(55) Geri, J. B.; Oakley, J. V.; Reyes-Robles, T.; Wang, T.; McCarver, S. J.; White, C. H.; Rodriguez-Rivera, F. P.; Parker, D. L., Jr; Hett, E. C.; Fadeyi, O. O.; Oslund, R. C.; MacMillan, D. W. C. Microenvironment mapping via Dexter energy transfer on immune cells. *Science* **2020**, *367* (6482), 1091−1097.
(56) Trowbridge, A. D.; Seath, C. P.; Rodriguez-Rivera, F. P.; Li, B. X.; Dul, B. E.; Schwaid, A. G.; Buksh, B. F.; Geri, J. B.; Oakley, J. V.; Fadeyi, O. O.; Oslund, R. C.; Ryu, K. A.; White, C.; Reyes-Robles, T.; Tawa, P.; Parker, D. L., Jr; MacMillan, D. W. C. Small molecule photocatalysis enables drug target identification via energy transfer. *Proc. Natl. Acad. Sci. U.S.A.* **2022**, *119* (34), No. e2208077119.
(57) Gao, Y.; Ma, M.; Li, W.; Lei, X. Chemoproteomics, A Broad Avenue to Target Deconvolution. *Adv. Sci.* **2024**, *11* (8), No. e2305608.
(58) Wang, J.; Chao, B.; Piesner, J.; Kelly, F.; Kaech Petrie, S.; Xiao, X.; Li, B. X. CG-SLENP: A chemical genetics strategy to selectively label existing proteins and newly synthesized proteins. *JACS Au* **2024**, *4*, 3146−3156.
(59) Eng, J. K.; Jahan, T. A.; Hoopmann, M. R. Comet: an open-source MS/MS sequence database search tool. *Proteomics* **2013**, *13* (1), 22−24.
(60) Wilmarth, P. A.; Riviere, M. A.; David, L. L. Techniques for accurate protein identification in shotgun proteomic studies of human, mouse, bovine, and chicken lenses. *J. Ocul. Biol. Dis. Infor.* **2009**, *2* (4), 223−234.
(61) Keller, A.; Nesvizhskii, A. I.; Kolker, E.; Aebersold, R. Empirical statistical model to estimate the accuracy of peptide identifications made by MS/MS and database search. *Anal. Chem.* **2002**, *74* (20), 5383−5392.

https://doi.org/10.1021/jacsau.4c00988
JACS Au 2025, 5, 302−319